






# Systematic Investigation of Very-early-phase Spectra of Type Ia Supernovae

Mao Ogawa<sup>1</sup> , Keiichi Maeda<sup>1</sup> , and Miho Kawabata<sup>2</sup> <sup>1</sup>Department of Astronomy, Kyoto University, Kitashirakawa-Oiwake-Cho, Sakyo-ku, Kyoto, 606-8502, Japan; [mao.ogawa@kusastro.kyoto-u.ac.jp](mailto:mao.ogawa@kusastro.kyoto-u.ac.jp), [keiichi.maeda@kusastro.kyoto-u.ac.jp](mailto:keiichi.maeda@kusastro.kyoto-u.ac.jp)<sup>2</sup>Nishi-Harima Astronomical Observatory, Center for Astronomy, University of Hyogo, 407-2 Nishigaichi, Sayo-cho, Sayo, Hyogo, 679-5313, Japan  
Received 2022 October 11; revised 2023 July 29; accepted 2023 July 31; published 2023 September 15

## Abstract

It has been widely accepted that Type Ia supernovae (SNe Ia) are thermonuclear explosions of a CO white dwarf. However, the natures of the progenitor system(s) and explosion mechanism(s) are still unclarified. Thanks to the recent development of transient observations, they are now frequently discovered shortly after the explosion, followed by rapid spectroscopic observations. In this study, by modeling very-early-phase spectra of SNe Ia, we try to constrain the explosion models of SNe Ia. By using the Monte Carlo radiation transfer code, TARDIS, we estimate the properties of their outermost ejecta. We find that the photospheric velocity of normal-velocity supernovae (NV SNe) in the first week is  $\sim 15,000 \text{ km s}^{-1}$ . The outer velocity, to which the carbon burning extends, spans the range between  $\sim 20,000$  and  $25,000 \text{ km s}^{-1}$ . The ejecta density of NV SNe also shows a large diversity. For high-velocity supernovae (HV SNe) and 1999aa-like SNe, the photospheric velocity is higher,  $\sim 20,000 \text{ km s}^{-1}$ . They have different photospheric densities, with HV SNe having higher densities than 1999aa-like SNe. For all these types, we show that the outermost composition is closely related to the outermost ejecta density; the carbon-burning layer and the unburnt carbon layer are found in the higher-density and lower-density objects, respectively. This finding suggests that there might be two sequences, the high-density and carbon-poor group (HV SNe and some NV SNe) and the low-density and carbon-rich group (1999aa-like and other NV SNe), which may be associated with different progenitor channels.

*Unified Astronomy Thesaurus concepts:* Type Ia supernovae (1728); Radiative transfer simulations (1967); White dwarf stars (1799)

## 1. Introduction

It has been widely accepted that Type Ia supernovae (SNe Ia) are thermonuclear explosions of a massive CO white dwarf (WD) in a binary system. They show a correlation between the peak luminosity and the light-curve timescale (Phillips 1993), with which SNe Ia can be used as reliable standardizable candles for cosmological measurements (Riess et al. 1998; Perlmutter et al. 1999).

However, the observational properties of SNe Ia are not uniform. Various sequences or subclasses have been identified (e.g., Branch et al. 2006). Classically, SNe Ia are placed on the peak-luminosity sequence, i.e., the 1991T-normal-1991bg sequence (Filippenko et al. 1992a, 1992b); 1991T-like SNe are brighter than  $-19.5$  mag at the peak, while 1991bg-like SNe can be fainter than  $-18.0$  mag. They also form a spectral sequence, associated with the photospheric temperature (Nugent et al. 1995). Additional diversity in the spectral properties within the normal class has also been discovered. Based on the velocity of Si II 6355 Å at the maximum-light phase, the normal class can be further divided into two types (Benetti et al. 2005; Wang et al. 2009); high-velocity (HV) SNe (with  $\gtrsim 12,000 \text{ km s}^{-1}$ ) and normal-velocity (NV) SNe (with  $\lesssim 12,000 \text{ km s}^{-1}$ ). The origins of these diversities have not yet been clarified.

The natures of the progenitor(s) and explosion mechanism(s) of SNe Ia are still unclarified. There are two popular scenarios for their progenitors; (1) the single-degenerate (SD) scenario in

which the WD mass approaches the Chandrasekhar mass ( $M_{\text{ch}}$ ) by accreting hydrogen or helium via binary mass transfer (Whelan & Iben 1973), and (2) the double-degenerate (DD) scenario in which merging two sub- $M_{\text{ch}}$  WDs leads to thermonuclear runaway (Iben & Tutukov 1984).

Regarding the explosion mechanisms, several models have been proposed. Classically, the delayed-detonation model of a  $M_{\text{ch}}$  WD has been considered a plausible model. In this model, carbon ignition occurs near the center of the progenitor, and the associated flame speed changes from subsonic (i.e., deflagration) to supersonic (detonation). A number of theoretical simulations have been performed (e.g., Khokhlov 1991; Hoefflich & Khokhlov 1996; Iwamoto et al. 1999; Röpke et al. 2007; Maeda et al. 2010a). As a global structure, the iron-group elements, such as  $^{56}\text{Ni}$  and  $^{58}\text{Ni}$ , are synthesized in the central region, while the lighter elements are distributed toward the outer region. The outermost region mostly consists of  $^{16}\text{O}$  due to the carbon burning, with little unburnt carbon; in the reference model CS15DD2 of Iwamoto et al. (1999),  $\sim 5 \times 10^{-3} M_{\odot}$  of the unburnt carbon are distributed at  $>30,000 \text{ km s}^{-1}$ . As the turbulence during deflagration creates a seed for the mixing structure (Seitenzahl et al. 2013), the onion-like structure described above is smoothed out to some extent in multidimensional simulations. In this model, the central density of the WD, the composition structure, and the condition of the deflagration-to-detonation transition (DDT) can potentially produce diversity in SNe Ia (e.g., Hoefflich & Khokhlov 1996; Iwamoto et al. 1999; Umeda et al. 1999). Moreover, as the central ignition is not necessarily spherically symmetric, a global asymmetry can be produced, which might contribute to observational diversity (Maeda et al. 2010b).

Another leading model is the sub- $M_{\text{ch}}$  WD double-detonation model, which has been under intensive investigation, especially in the last decade. In this model, the He detonation occurs first in the He shell on the surface of a sub- $M_{\text{ch}}$  CO WD, and the resulting shock wave triggers the carbon detonation near the center of the progenitor WD (e.g., Nomoto 1982; Hoefflich & Khokhlov 1996; Sim et al. 2010; Shen et al. 2021). Since the original suggestion (e.g., Nomoto 1982), the scenario had been relatively unexplored for several decades, as compared to the delayed-detonation model, mainly due to some shortcomings in the model to reproduce observational properties of normal SNe Ia (e.g., Hoefflich & Khokhlov 1996). However, the scenario has been revisited both theoretically (Fink et al. 2010; Shen et al. 2018; Iwata & Maeda 2022) and observationally (Jiang et al. 2017; Maeda et al. 2018; De et al. 2019) in the last decade. The double-detonation model has been theoretically investigated both by one-dimensional simulations (Sim et al. 2010; Woosley & Kasen 2011) and by multidimensional simulations (Fink et al. 2010; Tanikawa et al. 2018; Shen et al. 2021). In this model, the central region is dominated by  $^{56}\text{Ni}$  as the carbon detonation ash. The model has characteristic nucleosynthesis products in the outermost layer as a result of the He detonation; a large amount of unburnt He is left, with a small amount of intermediate-mass elements such as Si and Ca. Depending on the model details, the Fe-peak elements are also produced in the outermost layer. In the model by Shen et al. (2021), oxygen and unburnt carbon are distributed at  $15,000\text{--}20,000\text{ km s}^{-1}$  near the boundary between the He shell and CO core material. The variations in the CO core mass and He shell mass are expected in this scenario; the latter is dependent either on the mass accretion rate or the companion WD mass.

Spectroscopic observation is one of the most powerful methods to understand the nature of SNe. Thanks to the recent development of transient observations, there has been an increasing number of SNe Ia discovered shortly after the explosion and quickly followed by spectroscopic observations. Given that the photosphere generally recedes in the mass coordinate due to the expansion and the density decrease, the very-early-phase spectra trace the nature of the outermost layer (e.g., Kawabata et al. 2020); this is a place where we may begin to decode differences associated with different explosion models, e.g., the carbon content (see above). However, systematic investigation of the very-early-phase spectra through spectral modeling has been lacking, as very-early-phase spectroscopy has become feasible only recently. In addition, spectral modeling of SNe Ia has been frequently conducted for the detailed time sequence of individual objects (i.e., the “tomography;” Mazzali et al. 2014), the strategy which has been applied to a number of objects (e.g., Magee et al. 2017; Heringer et al. 2019; Barna et al. 2021; Aouad et al. 2022; O’Brien et al. 2023, for recent examples), but systematic investigation of a sample of spectra at similar epochs has been limited. The latter is our strategy in this work; by modeling spectra of SNe in the earliest phase ever possible and in a systematic manner, we aim at investigating the nature of the outermost layer, its diversity, and a possible relation to different progenitor and explosion scenarios.

Another issue related to the SN spectral synthesis study is the treatment of subjectivity and uncertainty in fitting the observational data, given the large degree of freedom involved in the spectral modeling. With the recent advances in computation

power coupled with a sophisticated method like machine learning, the possibility of an automated fitting procedure not involving human inspection starts attracting attention; such an approach has, for example, been realized by the construction of a synthetic-spectra emulator (Kerzendorf et al. 2021); it has been successfully applied to fit the observed spectrum of a single object (O’Brien et al. 2021), or recently to a spectral sequence of a group of objects (O’Brien et al. 2023). In the present work, we seek a complementary approach between the classical method (based on experts’ experience and visual inspection) and the modern method (based on automation).

In this study, we perform spectral synthesis calculations for very-early-phase spectra, taken within a week since the explosion, for 14 SNe Ia. In Section 2, we summarize the properties of the sample of SNe Ia that we compiled from the literature and describe the spectral fitting method. We present the results of the spectral synthesis calculations and the comparison to the observed spectra in Section 3. In Section 4, we discuss the nature of SNe Ia obtained through the density and composition structures, including a discussion on emerging subclasses and their possible connections to different progenitor/explosion mechanisms. Section 5 provides additional discussion. Our findings are summarized in Section 6.

## 2. Method

### 2.1. Sample Selection and Properties of 14 SNe Ia

A sample of the very-early-phase spectra of 14 SNe Ia has been constructed as follows. We here searched for objects that satisfy the following three criteria through the astrophysics data system (ADS)<sup>3</sup>; (1) spectra observed within 1 week since the explosion exist, (2) photometric data that cover the date when the spectrum was taken are available, and (3) the sources have been intensively observed around the maximum light so that the basic properties are well specified (e.g., the peak luminosity, SN Ia classification and subtype, and declining rate). We summarize the properties of these 14 SNe Ia in Table 1.

Table 2 summarizes the sources of the spectra modeled in the present study.<sup>4</sup> We first calibrate the observed flux with photometry data. The extinction is then corrected using the extinction law by Cardelli et al. (1989); it is performed for the Milky Way (with  $R_V = 3.1$ ) and the host galaxy separately (see Table 1). Finally, we convert the flux to luminosity using the distance modulus listed in Table 1. In addition, the wavelength is converted to the rest-frame wavelength.

### 2.2. Spectral Synthesis Calculation: TARDIS

To constrain the structure of the outermost ejecta of SNe Ia, we use a radiation transfer code, TARDIS (Kerzendorf & Sim 2014). For spherically symmetric and homologously expanding ejecta, TARDIS performs a radiative transport calculation by using the Monte Carlo method for photon packets originally emitted from a sharply defined photosphere. The input parameters are as follows; (1) the luminosity, (2) the photospheric velocity, (3) the density structure, (4) the abundance structure (after explosive nucleosynthesis), and (5) the time since the explosion. Following the photon

<sup>3</sup> <https://ui.adsabs.harvard.edu/>

<sup>4</sup> The spectra are downloaded from WISERep (Yaron & Gal-Yam 2012; <https://www.wiserep.org/>)

**Table 1**  
Properties of 14 SNe Ia Studied in the Present Work

Object	Type	$z$	$\mu$ (mag)	$E(B - V)_{\text{host}}$ (mag)	$R_V$	$E(B - V)_{\text{MW}}$ (mag)	$\Delta m_{15(B)}$ (mag)	Reference
2009ig	HV	0.00877	32.6	0.00625	1.6	0.089	0.89	Foley et al. (2012)
2011fe	NV	0.000804	29.04	0.032	3.1	0.008	1.18	Zhang et al. (2016b)
2012cg	99aa	0.00146	30.9	0.18	2.4 <sup>a</sup>	0.018	0.86	Silverman et al. (2012)
2012fr	NV	0.004	31.27	0.03	3.1	0.018	0.83 <sup>b</sup>	Contreras et al. (2018)
2012ht	NV	0.004	31.5	0	0	0.02	1.39	Yamanaka et al. (2014)
2013dy	NV	0.00389	31.49	0.15	3.1 <sup>c</sup>	0.15	0.89	Zheng et al. (2013)
2013gy	NV	0.0140	33.68	0.106	2.4 <sup>a</sup>	0.049	1.234	Holmbo et al. (2019)
2016coj	NV	0.005	31.9	0	3.1	0.02	1.25	Zheng et al. (2017)
2017cbv	99aa	0.00340	31.14	0	0	0.15	1.06	Hosseinzadeh et al. (2017)
2017cfd	NV	0.0121	33.52	0.1 <sup>d</sup>	1.7	0.02	1.16	Han et al. (2020)
2017fgc	HV	0.008	32.81	0.29	1.55	0.029	1.1	Burgaz et al. (2021)
2018gv	NV	0.0053	30.92 <sup>e</sup>	0.028	3.1	0.051	0.96	Yang et al. (2020)
2019ein	HV	0.00776	32.95	0.09	1.55	0.011	1.36	Pellegrino et al. (2020)
2019yvq	HV	0.00908	33.14	0.032	2.4	0.018	1.5	Miller et al. (2020)

**Notes.** The data come from the reference papers (ninth column) unless mentioned otherwise.

<sup>a</sup> Unless the value of  $R_V$  is discussed in the original reference, we adopt  $R_V = 2.4$  (see Wang et al. 2009).

<sup>b</sup> Cain et al. (2018).

<sup>c</sup> Pan et al. (2015).

<sup>d</sup> From Figure 5 of the reference paper, we adopt  $E(B - V)_{\text{host}} = 0.1$ .

<sup>e</sup> Nasonova et al. (2011).

**Table 2**  
Spectra Modeled in the Present Work

Object	Date	Phase <sup>a</sup> (day)	Reference
2009ig	2009-08-22	-14.2	Foley et al. (2012)
2011fe	2011-08-25	-16	Zhang et al. (2016b)
2012cg	2012-05-18	-14.8	Silverman et al. (2012)
2012fr	2012-10-28	-14.51	Childress et al. (2013)
2012ht	2012-12-20	-13.9	Yamanaka et al. (2014)
2013dy	2013-07-11	-16.07	Zheng et al. (2013)
2013gy	2013-12-7	-14.7	Holmbo et al. (2019)
2016coj	2019-05-28	-11	Zheng et al. (2017)
2017cbv	2017-03-10	-19	Hosseinzadeh et al. (2017)
2017cfd	2017-03-18	-13.2	Han et al. (2020)
2017fgc	2017-07-11	-13	Burgaz et al. (2021)
2018gv	2018-01-16	-15.5	Berton et al. (2018)
2019ein	2019-05-2	-14	Pellegrino et al. (2020)
2019yvq	2020-01-1	-12.94	Burke et al. (2021)

**Note.**

<sup>a</sup> The phase is the day measured from the maximum light.

propagation, the structures of the temperature and the excitation state of the elements are constructed so as to satisfy the thermal balance coupled with the determination of the ionization state through the ionization balance. Finally, the emerging spectrum is calculated.

We performed spectral synthesis calculations for various combinations of the input parameters to fit the observed spectrum. Our main goal is to constrain the density and the composition distributions in the outermost ejecta. As a general problem, the fit involves a large degree of freedom. In the present work, in order to simplify the problem, we adopt a single power-law density structure,  $\rho \propto v^{-\alpha}$  ( $\alpha = 4 \sim 14$ ), up to the outermost velocity (which is taken as a parameter together with  $\alpha$ ). We note that we have to introduce the outermost velocity cut in the density structure, as the single power-law

distribution alone does not take into account the sharp drop in the density in the outermost layer expected in (any) explosion models that connect the ejecta and the surrounding “vacuum.” For example, the W7 model (Nomoto et al. 1984) has a sharp drop in the density distribution at  $\sim 20,000 \text{ km s}^{-1}$ , above which there is essentially no ejecta material, while the single power law provides a reasonable approximation below it. The outermost velocity is usually not important in modeling the maximum-phase spectra, given that the photosphere has already receded deep inside; this is not the case if one starts studying the infant-phase spectra, aiming at investigating the outermost density structure, which is otherwise not accessible.

We further assume a uniform composition structure above the photosphere. In addition, based on nuclear physics, we consider only two characteristic layers: a carbon-burning layer and an unburnt C + O layer. In the carbon-burning layer, the mass fractions are set as follows; 0.6795(O), 0.15(Si), 0.09(Mg), 0.07(S), 0.01(Ar), and 0.0005(Ca). In the unburnt C + O layer, we adopt the following fractions; 0.475(C), 0.5(O), and 0.025(Ne). As the photosphere is near the surface of the ejecta in the very early phase, it is enough to consider these two outermost layers. Using these two layers, we mix the unburnt carbon layer and the carbon-burning layer in proportions of  $x$  and  $(1 - x)$ , respectively. Then, we change the mixing fraction,  $x$  (between 0 and 1), and make a uniform composition. Finally, we add the solar abundance to the elements with atomic numbers  $N = 12, 14, 16,$  and  $20\text{--}30$ .

Modeling a given spectrum is separated into two stages. As the first step, a search for a “rough” solution is performed in a manner similar to the classical approach with visual inspection. This is done by performing TARDIS simulations for (relatively coarse) grids of models in a large parameter space. The fitting results are checked through our fitting/comparison algorithms and visual inspection (see Section 2.3). Then we exclude the parameter space that is unlikely to produce a good match to the observed spectrum, and set new (finer) grids of models for the final spectral synthesis simulations; the number of final model



grids is typically  $\sim 2000$ – $3000$  for each spectrum, which allows the investigation with relatively moderate computational power.

The first step also serves to fix the values for the time since the explosion and luminosity in the TARDIS input parameters. For the time since the explosion, we first try to constrain the explosion date using the light-curve evolution. We assume the homologously expanding “fireball model” (Arnett 1982). We use the  $R$ -band magnitude (if not available, the  $r$ -band magnitude is used instead) and fit the flux ( $f$ ) by  $f \propto t^2$ , where  $t$  is the time since the explosion. In this light-curve fit, we use only the data points before  $-7.0$  days measured from the maximum light; this is a reasonable compromise between the assumption of the single power law and the sufficient number of data points. The light-curve fit result is used as an initial guess for the time since the explosion for the spectrum under consideration. However, the date estimated by the light-curve evolution sometimes shows discrepancy to the “spectral” phase (Mazzali et al. 2014). We thus allow it to change at increments of 0.5 days in the first step, to check if the spectral-fit quality is improved. A similar procedure is performed for the input luminosity. Through this process, we thus fix the time since the explosion and the luminosity, which are adopted in setting up the final model grids.

### 2.3. Fitting Procedure: Numerical Evaluation of the Quality of the Fit

In many previous works for SN spectral synthesis, the quality of the spectral fit was checked and the best-fit parameters were selected by visual inspection (e.g., Mazzali et al. 2014; Kwok et al. 2022). However, as the spectral synthesis calculation involves many parameters even for a simplified/idealized input model, we have decided to introduce an objectively-quantified index to justify the spectral fit and check for possible degeneracy between the parameters.

A powerful approach to fully replace the classical (human-based) method is the development of a spectral synthesis emulator (Kerzendorf et al. 2021) and the direct data cube comparison between models and an observed spectrum (O’Brien et al. 2021). If one wants to select a best-fit synthesis spectrum with a number of model parameters, one will need a huge number of spectral synthesis simulations. This can be reduced to a practically manageable number by introducing machine learning, i.e., an emulator. This is an approach adopted by O’Brien et al. (2021) to model a single spectrum of SN 2020bo. This is a powerful method, but for the present purpose it is useful to consider a complementary approach: (1) To model the number of observed spectra that cover a range of epochs and spectral features, a training set will need to be carefully constructed and investigated, which may require a huge number of spectral simulation calculations to train the emulator for practical application (but see, O’Brien et al. 2023, for a recent update along this line). (2) While the application of the emulator to the direct data cube fit to the data has been successful in obtaining overall properties, it has not been clarified whether such a method is sufficiently sensitive to pick up relatively weak features in the fit (such as S II and C II; see, e.g., Figure 2 of O’Brien et al. 2021); it is indeed a main interest in the present investigation.

We thus introduce our own-customized method for the fit of the model spectra to the observational spectra, based on the “preextracted features” that characterize the properties of SN spectra (which rely on the experiences of experts and our

experiment; see below). Rather than directly comparing the model and observed spectra both as a one-dimensional data set with thousands of data points as a function of the wavelength, we have decided to extract some characteristic spectral features as motivated by the physics of spectral formation. The first item then is to decide which “observational” features to fit. We have tested various observational quantities as follows; first we have evaluated how well an observed spectrum matches a TARDIS model spectrum, solely based on the fit between the characteristic quantities under consideration, which are extracted both from the observed spectrum and the TARDIS model using the same scheme. The result is then checked by visual inspection of the match directly between the observed and model spectra. By repeating these procedures, we have decided to adopt the following items; (a) the velocity minimum ( $\lambda_{\min}$ ) of each absorption line, (b) the equivalent width (EW) of each absorption line, (c) the FWHM of each absorption line, and (d) the color of the spectrum (Col). The absorption lines adopted for tests (a)–(c) are as follows; (1) Fe II & Fe III 4500 Å, (2) Fe II & Fe III 5200 Å, (3) S II 5454 Å, (4) S II 5620 Å, (5) Si II 5972 Å, (6) Si II 6355 Å, and (7) C II 6578 Å.

For an observational spectrum, the properties of the lines (e.g., EWs) are extracted as follows. First, we provide a guess of the blue and red edges of each absorption line in the wavelength by visual inspection. We then numerically search for the wavelength at which the flux has the maximum value (i.e., the true edge) within 30 Å around the initial guess, for both the blue and red sides. The imposed range of 30 Å is sufficient as it corresponds to  $\sim 1,500$  km s $^{-1}$ , which is larger than the accuracy of the initial guess through the visual inspection. A continuum is set as a straight line connecting the blue and red edges of each absorption line, following the standard procedure to compute the “pseudo” EWs (e.g., Hachinger et al. 2008; Zhao et al. 2015; Modjaz et al. 2016). Then, a normalized line profile is constructed by using the continuum for each absorption line, which is finally used to define (a)  $\lambda_{\min\text{obs}}(i)$  (the velocity at the absorption minimum), (b)  $\text{EW}_{\text{obs}}(i)$  (the equivalent width), and (c)  $\text{FWHM}_{\text{obs}}(i)$  (the line width), where the index  $i$  (from 1 through 7) refers to the different absorption lines (see above). For the color (item d), denoted as  $\text{Col}_{\text{obs}}$ , we calculate the slope of the line connecting the flux at the red edge of the Fe II & Fe III 5200 Å feature and the flux at 6700 Å. Note that the detail in the determination of the continuum (a straight-line continuum in this case) is not a concern; the key is that the same procedure is applied to the observed and model spectra under comparison (see below) so that the fit can be numerically evaluated on the same basis. The same argument also applies to using the “pseudo” EWs as the fit quantities.

Essentially the same procedures are adopted for the TARDIS model spectra, where the initial guesses for the edges of the absorption lines are taken from the corresponding “true” edges of the observed spectra. Applying the “observationally” determined positions as the initial guess is justified, given our purpose of selecting model spectra that fit the observed one; if a model spectrum has the characteristic wavelengths of the line profiles outside the searched range, such a spectrum is considered to provide a bad fit in the fitting procedure described below. We then obtain the spectral properties for the model spectra, i.e.,  $\lambda_{\min\text{TAR}}(i)$ ,  $\text{EW}_{\text{TAR}}(i)$ ,  $\text{FWHM}_{\text{TAR}}(i)$ , and  $\text{Col}_{\text{TAR}}$ .

To evaluate the quality of the fit between an observed spectrum and a model spectrum, we then introduce weight

parameters  $W_i$  ( $i = 1-7$ ) for each element, as shown below. We test various combinations of  $W_i$  so that the following numerical fits reproduce the result of visual inspection reasonably well (see below). For (a), the quality of the fit for each line is defined as follows (which is smaller for a better fit);

$$E_a(i) = \left( \frac{\lambda_{\text{minTAR}}(i) - \lambda_{\text{minobs}}(i)}{\Delta_i} \right)^2, \quad (1)$$

$$\Delta_i = \frac{\lambda_{\text{minobs}}(i) \times 2,000 \text{ km s}^{-1}}{c}, \quad (2)$$

where  $c = 3 \times 10^5 \text{ km s}^{-1}$  (speed of light).  $\Delta_i$  is a normalized constant; if the difference in the velocity of the absorption minimum between the observed spectrum and the TARDIS model spectrum is  $2,000 \text{ km s}^{-1}$ ,  $E_a(i)$  is equal to 1. By summing up  $E_a(i)$  for all the lines in the fit ( $i = 1 - 7$ ) with the corresponding weight parameter, we obtain the following;

$$E_{a\text{-tot}} = \sum_i E_a(i) \times W_i. \quad (3)$$

For (b), the quality of the fit is evaluated as follows;

$$E_b(i) = \begin{cases} \left( \frac{\text{nEW}_{\text{TAR}}(i) - \text{nEW}_{\text{obs}}(i)}{\text{nEW}_{\text{obs}}(i)} \right)^2 & (i \neq 6), \\ \left( \frac{\text{EW}_{\text{TAR}}(i) - \text{EW}_{\text{obs}}(i)}{\text{EW}_{\text{obs}}(i)} \right)^2 & (i = 6), \end{cases} \quad (4)$$

where

$$\text{nEW}_k(i) = \text{EW}_k(i) / \text{EW}_k(6). \quad (5)$$

Namely, the EWs are normalized by the EW of Si II 6355 Å in the fit. Then,

$$E_{b\text{-tot}} = \sum_i E_b(i) \times W_i. \quad (6)$$

For (c), the quality of the fit is evaluated as follows;

$$E_c(i) = \left( \frac{\text{FWHM}_{\text{TAR}}(i) - \text{FWHM}_{\text{obs}}(i)}{\text{FWHM}_{\text{obs}}(i)} \right)^2, \quad (7)$$

$$E_{c\text{-tot}} = \sum_i E_c(i) \times W_i. \quad (8)$$

For (d), the quality of the fit is evaluated as follows;

$$E_d = \left( \frac{\text{Col}_{\text{TAR}} - \text{Col}_{\text{obs}}}{\text{Col}_{\text{obs}}} \right)^2. \quad (9)$$

By adding all the contributions by items (a)–(d), we further introduce additional weight parameters,  $W'_\alpha$  ( $\alpha = \{a, b, c, d\}$ ). We then combine the fitting residuals computed for different features associated with different lines as follows;

$$E_{\text{total}} = \sum_{\alpha=a-d} W'_\alpha \times E_\alpha. \quad (10)$$

We note that the values of  $W'_\alpha$  do not necessarily measure the relative importance of different items in the fit; they are coupled with the normalization in the corresponding  $E_\alpha$ .

Through the above procedures, we find that a group of model spectra, which have too weak/shallow absorption lines but at the correct positions, are not always rejected, while they clearly do not provide a good match to the observed spectra by visual inspection. Rather than tuning the relative weight between the

**Table 3**  
Weight Parameters

Index	$W_i$	Index	$W'_\alpha$
1	0.5	a	1
2	0.5	b	0.06
3	0.2	c	0.05
4	0.3	d	0.01
5	1	e	0.5
6	1		
7	0.7		

**Note.** These are set the same for all the objects.

velocity minima (item a) and the EWs (item b) of individual line features, we find it easy to automatically reject these models by introducing another criterion of the “total EW” for each spectrum. We thus compute the sum of the EWs of individual line features in each model spectrum and compare it to the corresponding value in the observed spectrum to fit. When the ratio of the model value to the observed one is smaller than the additional parameter  $W'_e$  (taken to be 0.5), the model spectrum is judged to be “too smooth.” In this case, the  $E_{\text{total}}$  is added by 30; this value is arbitrary but set so that the model spectrum is essentially judged as unacceptable.

With this additional constraint, the final value of  $E_{\text{total}}$  is given as follows;

$$E_{\text{total}} = \sum_{\alpha=a-d} W'_\alpha \times E_\alpha + P, \quad (11)$$

$$P = \begin{cases} 30 & \left( \frac{\sum_i \text{EW}_{\text{TAR}}(i)}{\sum_i \text{EW}_{\text{obs}}(i)} < W'_e \right) \\ 0 & \left( \frac{\sum_i \text{EW}_{\text{TAR}}(i)}{\sum_i \text{EW}_{\text{obs}}(i)} > W'_e \right) \end{cases}. \quad (12)$$

We regard that the quality of the fit is better for a model with a smaller value of  $E_{\text{tot}}$ .

The procedure here applies to given model grids and an observed spectrum, once the weight parameters are given. The weight parameters are introduced so that the numerical fit can reproduce the result of visual inspection, i.e., they must be set so that  $E_{\text{total}}$  is smaller for spectra that are judged to provide a better fit though visual inspection. This is difficult to numerically quantify and necessarily involves subjectivity. We have done it through trial and error using the spectrum of SN 2011fe as test data. For a given model grid, we have selected a group of “good-fit” spectra through visual inspection. Then, we search for the combination of the weight parameters so these models are selected in the top 3% in the agreement with the observed spectrum. This procedure is repeated several times as the initial guess in the first step also uses information obtained by the numerical fit. The values of the weight parameters thus obtained are shown in Table 3. We find that the same set of the weight parameters applies to the spectra of the other SNe investigated in the present sample; thus we use the same weight values throughout the analyses in the present work. This suggests that the procedure here is rather generic and can potentially be expanded into a sample of SNe with different phases.

### 3. Results

Figure 1 shows the results of the spectral synthesis calculations. The fitting procedure is constructed in such a way that a weight is given to the line features, i.e., the positions of the absorption minima, the depths, and the widths, followed by the continuum color. This is partly because the normalization of the spectra is highly uncertainty due to the interstellar extinction, while the properties of the absorption lines are not sensitively affected. Furthermore, the line features contain a wealth of information about the spectral formation process, thus strongly reflecting the nature of supernovae. These best-fit spectra match the properties of Si II 6355 Å, the “w” feature of S II 5606 & 5640 Å, as well as C II 6578 (when it is robustly detected in the observed spectra). Note that in this study, we do not try to fit the Ca II near-infrared triplet because it is very sensitive to temperature and therefore to a detailed treatment of microphysics like the non-LTE effect (Kasen 2006). O I 7774 Å is contaminated by Ca II, and thus it is also omitted from the fit.

Table 4 shows the parameters for the best-fit model selected for each object (Figure 1). These models are selected as follows. For each object, we rank all the models according to the value of  $E_{\text{total}}$  in the fit, which is numerically (and automatically) obtained. The models that are in the top 3% in the fitting rank (small  $E_{\text{total}}$ ) are grouped as the best-fit “candidates” (or acceptable models). Then we calculate the “pass rate” for each parameter, which is defined as the number of acceptable models (i.e., the best-fit candidates within the top 3%) divided by the number of all the trials for each parameter value under consideration. As the pass rate corresponds to a probability density, the “best-fit” value for that parameter is considered to be near the peak of the pass-rate distribution. We decided to adopt the “mode” in the distribution for each parameter as the corresponding best-fit value.

As the numerical evaluation of the fit is aimed to be a simplified (and automatic) algorithm to “mimic” the visual inspection, it sometimes cannot recognize apparently slight absorption lines such as C II. We thus perform an additional selection procedure based on visual inspection, as follows. The best-fit values for the parameters “except for the fraction of the CO layer” are taken as the mode values in the pass-rate distribution for each parameter (see above). For this parameter set, we pick a model series for which only the fraction of the CO layer is varied. We then select the best-fit model by visual inspection between this model series and the observed spectrum under consideration. This way, we constrain the fraction of the CO layer separately from the other parameters.

Note that the best-fit models shown in Figure 1 are not always the ones with the smallest  $E_{\text{total}}$ , following the steps of the selection procedures as described above. We emphasize that our procedure provides a way to measure the error and uncertainty associated with each parameter by inspecting the range of the parameter sets in the acceptable or unacceptable groups. Our procedure thus enhances reproducibility; the evaluation of the fit is not too arbitrary nor too biased by the experience of individual researchers, as the best-fit value for each parameter (except for the fraction of the CO layer) is determined by the automatic evaluation processes (for which the details of the algorithm are presented and can be reproduced); the fraction of the CO layer involves visual inspection, but it is done with the other parameters automatically fixed and thus the degree of freedom in the fit has been already reduced substantially.

#### 3.1. An Example of the Best-fit Model: SN 2011fe

In this work, as we use the numerical test for the quality of fit, we can discuss the uniqueness and uncertainty of the best-fit parameters. To illustrate this point, in this section we introduce the results of our fitting algorithm for a specific example, SN 2011fe. In the second step for SN 2011fe, we calculate 2699 models in total and define the group of models that belong to the top 3% in the fitting agreement that pass the automatic screening (i.e., “the best-fit candidates” or “acceptable models”). The result is shown in Figure 2. In the left panels, we show the distributions of the number of models that we have calculated (blue) and the number of the models that pass the screening (orange), for some selected parameters. In the right panels, we show the distribution of the “pass rate,” defined as the number of acceptable models divided by the number of all the trials for each parameter value. We also calculate an error for each parameter, which is defined as a  $1\sigma$  confidence interval from the mode in the pass-rate distribution.

With the best-fit parameters (except for the fraction of the CO layer) fixed as the mode values in the pass-rate distributions, we then perform the additional selection regarding the C II absorption line based on visual inspection. Figure 3 shows the spectra for this final model sequence (varying the fraction of the CO layer) as compared to the spectrum of SN 2011fe. Through visual inspection, we regard the best-fit model as the one with a fraction of the CO layer of 0.8. As mentioned above, the best-fit model is not necessarily the one with the smallest  $E_{\text{total}}$ . The best-fit model adopted for SN 2011fe through the above processes is ranked 19th in terms of  $E_{\text{total}}$  among the 2699 models (i.e., in the top 0.7%).

According to Figure 2, we find that the photospheric density, the location of the photosphere ( $v_{\text{ph}}$ ), and the photospheric temperature are very well determined. In general, the density and the abundance can degenerate. However, by focusing on the very-early-phase spectra, we can place a reasonable assumption that the abundance is well represented by the C + O unburnt layer and/or carbon-burning layer. This is how the photospheric density and the abundance are separately constrained in the present study. On the other hand, it turns out that the density gradient is not so strongly constrained. This is because information near the photosphere mainly contributes to the shape of the spectral feature. As the photospheric temperature is well constrained by the ionization and excitation conditions, together with the continuum color, the luminosity is tightly constrained by the overall flux level.

#### 3.2. Summary of the Fits to the Entire Sample

Table 5 summarizes the results of the numerical evaluation for all the objects. NV SNe tend to have small values for minimum  $E_{\text{total}}$  except for SN 2012fr, which we discuss further in Section 4.2. On the other hand, HV SNe and 1999aa-like SNe tend to have relatively high values of the minimum  $E_{\text{total}}$ , as compared to NV SNe. This might suggest that some of the assumptions in the model construction are worse in the high-velocity ejecta found in these subclasses than in the low-velocity ejecta found in NV SNe. One possibility is the assumption of a single power-law density distribution, which we plan to investigate in the future.

In any case, given that the model parameters (e.g., the density, velocity, and composition) are reasonably well constrained under the present model framework (Section 3.1),

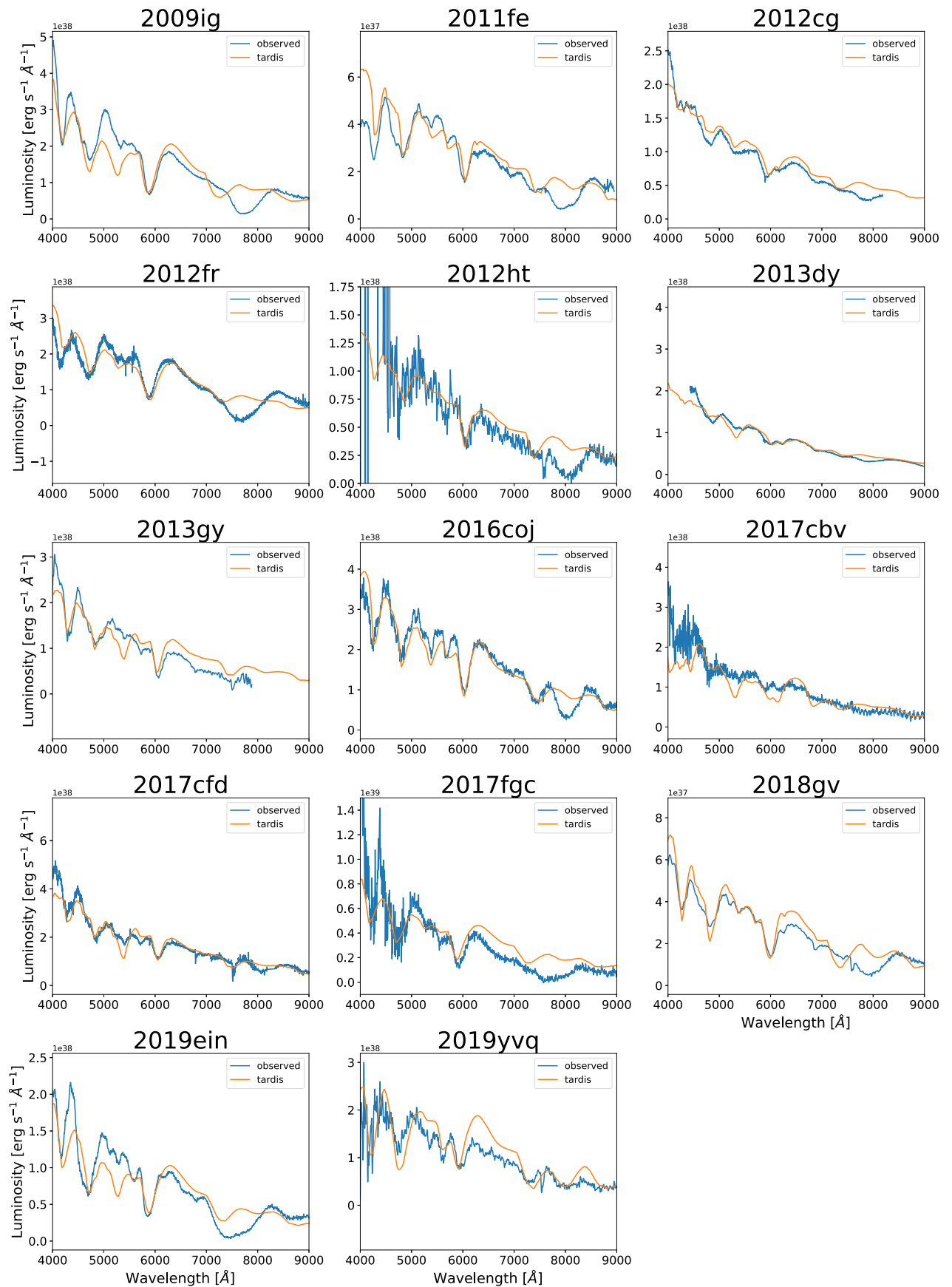


**Figure 1.** Comparison between the observed spectrum and the TARDIS model spectrum for each object. In each panel, the blue line is the observed spectrum, and the orange one is the TARDIS model spectrum.



**Table 4**  
TARDIS Parameters for the Early-phase Spectra of 14 SNe Ia

Object	Time Since the Explosion (day)	Luminosity ( $\log(L_{\odot})$ )	Photospheric Velocity ( $\text{km s}^{-1}$ )	Outer Velocity ( $\text{km s}^{-1}$ )	Photospheric Density* ( $10^{-16} \text{ g cm}^{-3}$ )	$\alpha$	Fraction of the C + O Unburnt Layer	Photospheric Temperature (K)
2009ig	3.9	8.55	19,000(1271)	31,000	$9.19_{5.22}^{12.31}$	4(1.6)	$0.00_{0.00}^{0.10}$	9933(2960)
2011fe	2.5	7.80	14,000(0)	24,000	$9.94_{5.31}^{11.56}$	12(2.9)	$0.70_{0.20}^{0.10}$	9778(310)
2012cg	2.9	8.35	19,000(1285)	31,000	$6.07_{4.38}^{15.73}$	10(2.1)	$0.70_{0.20}^{0.10}$	8124(0)
2012fr	3.7	8.50	20,000(771)	35,000	$6.23_{5.75}^{75.47}$	8(2.4)	$0.00_{0.00}^{0.10}$	9873(6214)
2012ht	3.4	8.15	15,000(410)	21,000	$3.82_{2.20}^{5.22}$	4(2.4)	$0.80_{0.30}^{0.00}$	9304(339)
2013dy	2.6	8.45	16,000(803)	30,000	$3.45_{2.62}^{11.05}$	8(2.8)	$0.05_{0.00}^{0.05}$	12539(2471)
2013gy	4.1	8.40	14,000(542)	21,000	$13.5_{4.2}^{6.2}$	8(3.2)	$0.05_{0.05}^{0.00}$	10206(246)
2016coj	5.5	8.60	15,000(183)	23,000	$25.8_{10.7}^{18.5}$	10(2.4)	$0.00_{0.00}^{0.05}$	9447(233)
2017cbv	3.0	8.45	17,000(1135)	31,000	$13.6_{7.2}^{15.1}$	8(1.5)	$0.50_{0.00}^{0.20}$	11558(1560)
2017cfd	4.9	8.70	14,000(594)	21,000	$37.1_{14.2}^{22.5}$	10(2.2)	$0.01_{0.00}^{0.09}$	11260(690)
2017fgc	6.1	8.90	21,000(702)	30,000	$17.4_{4.3}^{5.9}$	6(1.5)	$0.00_{0.00}^{0.30}$	9049(232)
2018gv	2.5	7.80	14,000(756)	26,000	$4.92_{2.26}^{4.16}$	6(1.8)	$0.70_{0.20}^{0.20}$	9445(429)
2019ein	2.6	8.25	20,000(1111)	30,000	$5.54_{3.44}^{9.06}$	8(2.0)	$0.00_{0.00}^{0.05}$	9977(2786)
2019yvu	4.8	8.40	19,000(780)	28,000	$27.5_{11.0}^{18.5}$	10(2.1)	$0.00_{0.00}^{0.30}$	8799(513)

**Notes.** The numbers in parentheses correspond to  $1\sigma$  statistical uncertainties. The subscript and superscript values represent the lower and upper  $1\sigma$  statistical errors, respectively. The photospheric density is normalized to the corresponding value 20 days since the explosion.

it is unlikely that these are affected much by introducing a more complicated model structure. In addition, the difference in the distribution in the minimal  $E_{\text{total}}$  is just indicative, and further investigation of this possible difference will require enlarging the observational sample.

### 3.3. Density Structure

Figure 4 shows the density structures of the best-fit models for the 14 SNe Ia with the estimated error/uncertainty, as obtained by the TARDIS modeling. The figure is separated into three panels for different subclasses. In the NV SNe, the photospheric velocity is confined at  $\sim 15,000 \text{ km s}^{-1}$ . The outermost velocity, which corresponds to the region to which the carbon burning extends, shows variation from  $\sim 20,000 \text{ km s}^{-1}$  to  $\sim 25,000 \text{ km s}^{-1}$ . The ejecta density also shows diversity of nearly an order of magnitude.

The velocity range found for the HV SNe and 1999aa-like SNe is largely overlapping; the photospheric velocity and the outermost velocity are  $\sim 20,000 \text{ km s}^{-1}$  and  $\sim 30,000 \text{ km s}^{-1}$ , respectively, which are both higher than those of the NV SNe. The high velocity derived for the HV SNe is also consistent with the high velocity seen in the Ca II NIR triplet (Li et al. 2021). The ejecta densities span a similar range to that covered by the NV SNe, between  $\sim 10^{-15}$  (at the photosphere) and  $10^{-17} \text{ g cm}^{-3}$  (at the outermost edge), once scaled at 20 days since the explosion. As a combination of the HV SNe and 1999aa-like SNe, the range of the density “scale,” i.e., the density at the photosphere scaled at 20 days, is also similar to that found for the NV SNe (about an order of magnitude). Interestingly, we can discern the potential difference in the densities between the HV SNe and 1999aa-like SNe; the typical density of the HV SNe is higher than that of the 1999aa-like SNe. This is discussed further in Section 4.1. In summary, we find that the outermost density structures are distinct for different subclasses of SNe Ia.

### 3.4. Composition Structure

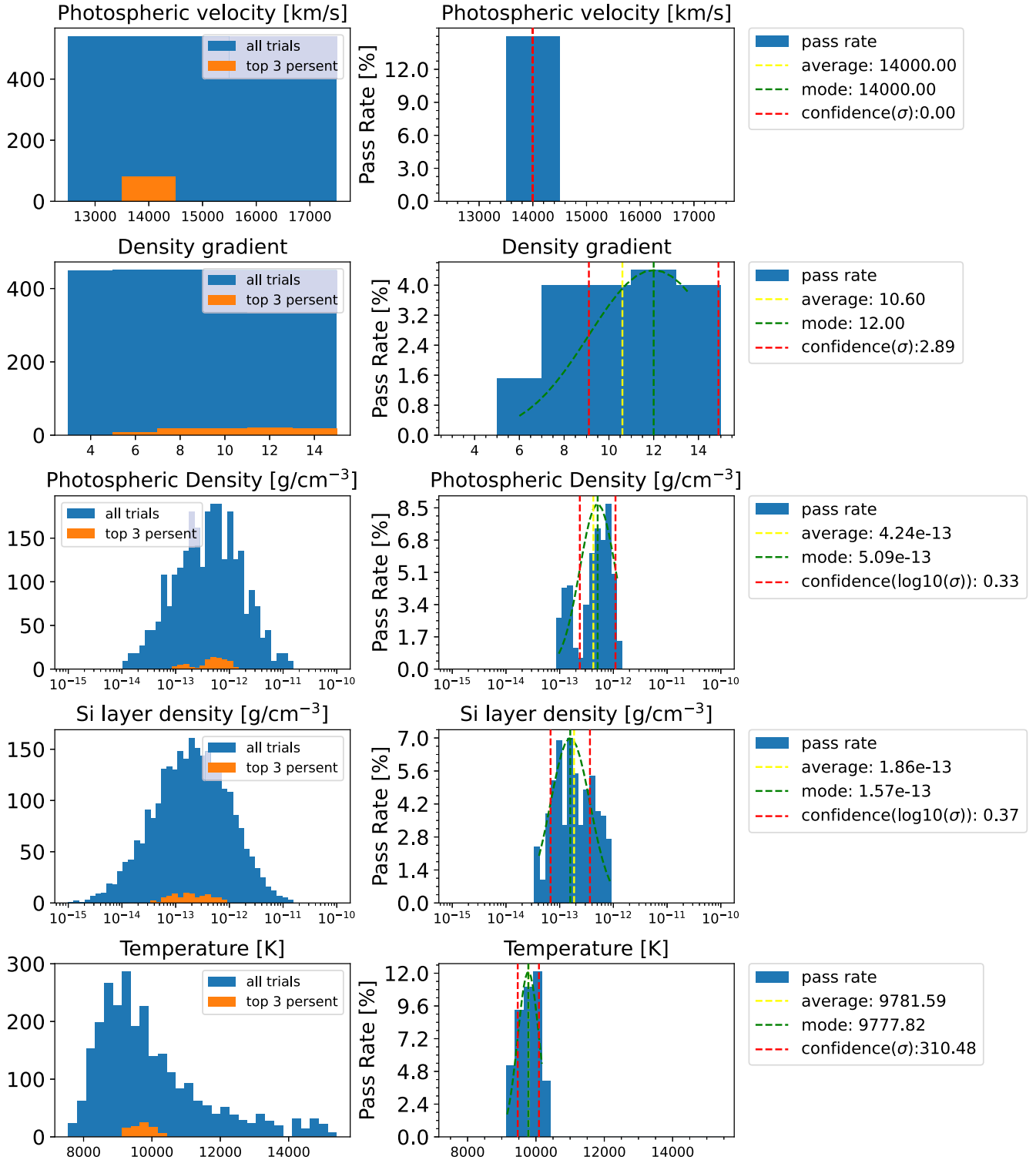
Figure 5 shows the fraction of the unburnt C+O layer contained in the outermost ejecta as constrained by the earliest spectra available for each object. In the 1999aa-like objects, we find that the fraction of the unburnt C+O layer is  $\sim 0.6$ . This means that the outermost layer is basically the unburnt C+O layer, and it is mixed by a small amount of the carbon-burning layer. The situation is the opposite for the HV SNe, for which the fraction of the C+O layer is essentially zero. Namely, the outermost layer of the HV SNe is represented by the carbon-burning composition (see also Li et al. 2021). We find that the NV SNe are divided into two groups in the composition of the outermost layer; one with a large fraction of the unburnt C+O layer and the other dominated by the carbon-burning layer.<sup>5</sup> The relation between the different subclasses and the fraction of the CO layer is further discussed in Section 4.1.

Table 6 shows the carbon masses contained in the best-fit models. Note that the values here are the lower limits because there could be additional carbon either above or below the velocity range constrained by the present models. First, there could be a pure C+O unburnt layer outside the ejecta shell modeled in this study. However, this contribution is probably negligible; we model the very-early-phase spectra, and the amount of material above the outermost velocity in our models should be very small given the steep density structure. On the other hand, the potential existence of carbon below the photosphere is not rejected by this study. This contribution should be negligible for the objects showing a carbon-poor composition in the outermost layer. For the objects showing a large fraction of the unburnt carbon layer (1999aa-like and some NV SNe), the carbon masses in Table 6 are likely underestimated.

<sup>5</sup> Note that we select the model showing C II for SN 2011ht, although the large noise level seen in the observed spectrum does not allow clear identification of C II; we see C II in this spectrum once it is smoothed, and the line is clearly seen in a spectrum taken 2 days after.



# SN 2011fe (pass rate: 3%)



**Figure 2.** The left panels show the distributions of the number of all the trials (blue) and the number of acceptable models (those in the top 3% in agreement with the observed one; orange), for each parameter. The right panels show the distribution of the “pass rate,” with a  $1\sigma$  confidence interval (red dashed line).

Those with carbon-rich composition (1999aa-like SNe and some NV SNe) have carbon masses of  $\gtrsim 0.001\text{--}0.01M_{\odot}$  (noting that these are the lower limits). On the other hand, those with carbon-poor composition (HV SNe and other NV SNe) have

carbon masses of  $\lesssim 0.001M_{\odot}$  (with only the exception of SN 2019ein). Therefore, these two groups, divided by the content of the unburnt carbon layer, are also distinct in terms of the carbon masses.

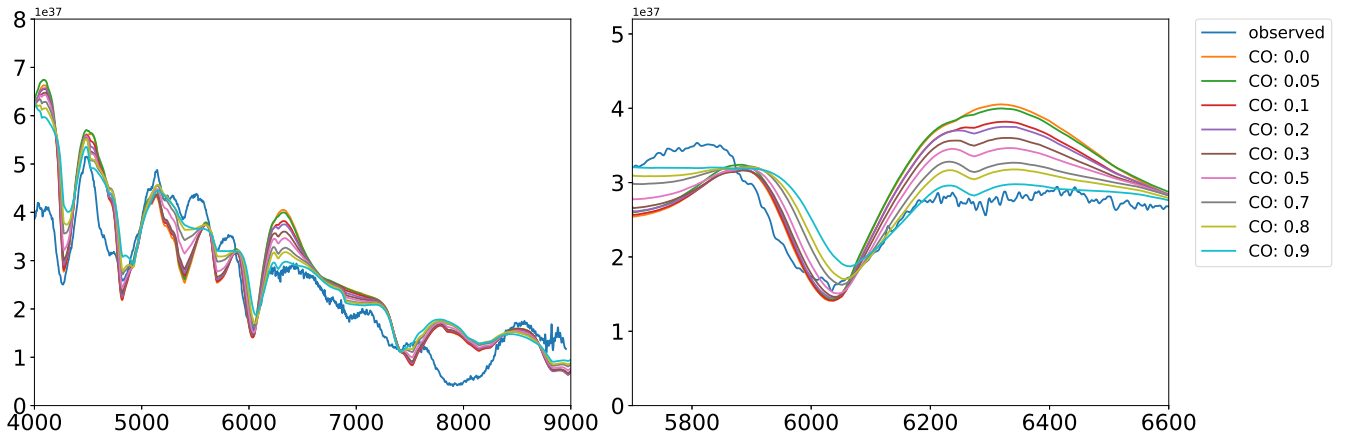


**Figure 3.** The left panel shows the spectra with the “best-fit” value for each parameter except for the fraction of the CO layer, showing how the amount of the CO layer affects the spectrum. The right panel is an expanded view around C II.

**Table 5**  
Numerical Analysis

Object	Number of Trials	Number of Top 5% Models	Minimum $E_{\text{total}}$
2009ig	2915	87	2.6777
2011fe	2699	80	0.2182
2012cg	2577	77	1.5411
2012fr	1889	56	3.2501
2012ht	1889	56	0.8045
2013dy	1889	56	0.4637
2013gy	1919	57	1.0206
2016coj	1919	57	0.5107
2017cbv	1943	58	2.2982
2017efd	2159	64	0.2812
2017fgc	2159	64	3.2283
2018gv	2302	69	0.6455
2019ein	1917	57	1.9852
2019yvq	2303	69	1.1558

## 4. Insights into the Nature of SNe Ia

### 4.1. Two Sequences in SN Ia Populations

In Sections 3.3 and 3.4, we have shown that HV SNe and 99aa-like SNe have different characteristics in the outermost density and composition, despite the similar velocity range found for the outermost ejecta. In Section 3.4, we have further shown that NV SNe could be divided into two classes based on the composition structure in the outermost ejecta; one dominated by the unburnt C+O composition and the other showing little trace of the unburnt C+O layer. The division between the two classes is also related to the outermost density (Section 3.3).

To further quantify these points, Figure 6 shows the characteristic density (scaled for the same epoch for all the SNe), as compared to the fraction of the CO layer for the 14 SNe. The characteristic density is defined as that at 16,000 km s<sup>-1</sup> (for NV SNe) or 21,000 km s<sup>-1</sup> (for HV SNe and 99aa-like SNe), i.e., just above the photosphere. Figure 7 summarizes how the fraction of the CO layer and the characteristic density are related to different subgroups; HV SNe versus 99aa-like SNe, and further NV SNe are divided into two subclasses (C-rich and C-poor; see below). According to the Student’s t-test, the chance probability with which the distribution of the CO fraction of the HV SNe and that of the 99aa-like SNe are

derived from the same parent population is  $\sim 6.0\%$ . The same chance probability for the distribution of the characteristic density is also  $\sim 6.0\%$ . While the sample size is still small, the difference between HV SNe and 99aa-like SNe is clearly indicated.

The density of the NV SNe with small unburnt C+O composition is as high as that found for HV SNe. This group may be regarded as a low-velocity analog of HV SNe, which also show both high density and little contamination of the unburnt C+O layer. On the other hand, the density seen in the group of the NV SNe with large amounts of unburnt C+O in the outermost layer is not as high as that of HV SNe. Interestingly, these features exhibited by this carbon-rich NV group are similar to those of 1999aa-like SNe, except for the difference in the velocity; this group may be regarded as a low-velocity analog of 1999aa-like SNe. By dividing the NV SNe into two classes based on the fraction of the CO layer (those with fractions  $>0.5$  and those with fractions  $<0.1$ <sup>6</sup>), we see a clear difference between the two groups (Figure 7). In terms of the fraction of the CO layer, the possibility that the two groups are derived from the same parent population is  $\sim 2.5\%$ , and the same probability is  $\sim 9.3\%$  for the characteristic density.

Therefore, we propose that NV SNe may be divided into two populations and that SNe Ia might be divided into two sequences; one is the NV–HV sequence and the other is the NV–1991T/1999aa-like sequence. The former sequence is characterized by high density and small amount of unburnt C+O later in the outermost ejecta (which might be linked to a similar suggestion by Li et al. 2021 based on observational properties); the latter sequence has lower density than the NV–HV sequence, and the outermost layer is dominated by unburnt C+O. Further investigating other observational properties in view of the proposed two populations should be interesting; for example, the HV SNe show a high polarization level around the maximum light (e.g., Maeda et al. 2010), and indeed SNe Ia might be divided into two groups in which one shows a high polarization degree (including HV SNe) and the other shows a low polarization degree (including 1991T-like SNe) (Meng et al. 2017).

<sup>6</sup> We however group SN 2013dy into the “carbon-rich” 99aa-like analog despite its low CO fraction, following the discussion in Section 4.3.

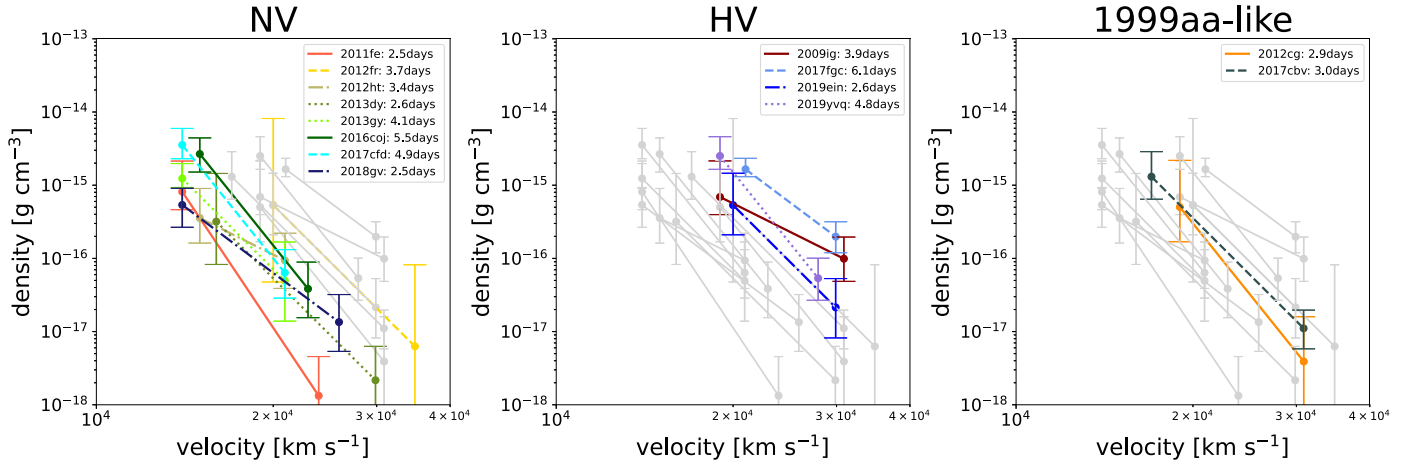


**Figure 4.** Density structure of each object based on the best-fit TARDIS model. The error bars in the density attached at the innermost and outermost velocities for each object represent the  $1\sigma$  confidence interval (see the main text).

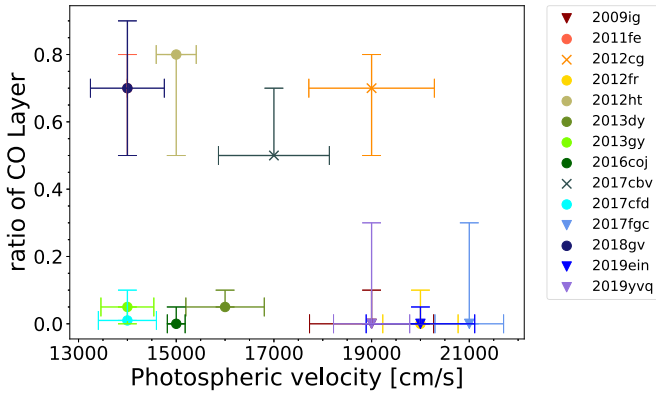


**Figure 5.** Fraction of the unburnt C + O layer to the total composition. The circles represent the NV type, the inverse triangles are for the HV type, and the crosses correspond to the 1999aa-like type. The error bars are obtained by the additional visual-inspection process to constrain the fraction of the CO layer, where only this parameter is varied while the other parameters are fixed to the best-fit values (see Section 3.1).

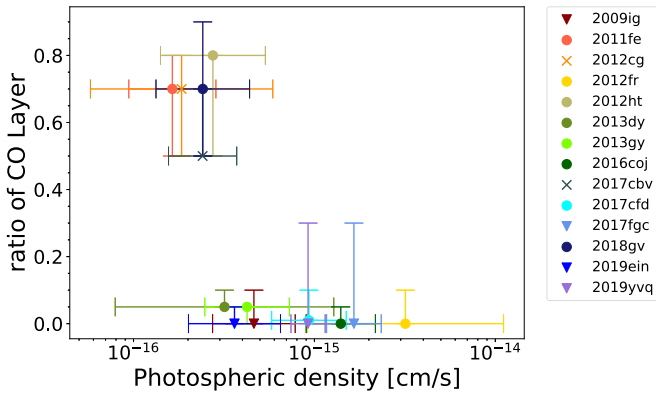


**Figure 6.** Characteristic density as compared to the fraction of the CO layer for the 14 SNe. The density is scaled at  $16,000 \text{ km s}^{-1}$  (for NV SNe) or  $21,000 \text{ km s}^{-1}$  (for HV SNe and 99aa-like SNe, respectively).

#### 4.2. SN 2012fr as a Transitional Case in the NV–HV Sequence

We find two outliers in the NV SN category, for which the outermost velocity is substantially higher than the other NV SNe Ia, noting that the NV classification is based on the maximum-light spectra. SN 2012fr is one such example. Despite its being classified as an NV SN, Childress et al. (2013)

**Table 6**  
Carbon Mass

Object	Carbon Mass ( $M_{\odot}$ )	Total Mass ( $M_{\odot}$ )
2009ig	0	0.059693535
2011fe	0.002747892	0.008292515
2012cg	0.00524938	0.015841442
2012fr	0	0.02665105
2012ht	0.004208668	0.011113205
2013dy	0.000197021	0.008323906
2013gy	0.000458434	0.019368311
2016coj	0	0.040493987
2017cbv	0.009617398	0.040632383
2017cfd	0.000204989	0.043302796
2017fgc	0	0.109386767
2018gv	0.00454342	0.013711013
2019ein	0	0.02441424
2019yvq	0	0.075874934

**Note.** The carbon mass and the total mass in the outermost ejecta studied in this work.

showed that the Si II 6355 and Ca II infrared triplets seen in SN 2012fr consist of a strong high-velocity feature (HVF) component in the early phase, which disappears toward the maximum phase. The maximum-light spectra are dominated by a slower, “photospheric” component and resemble those of other NV SNe. The density and composition structures derived in this study are very close to those of the HV SNe. The density in the outermost layer of SN 2012fr is as high as that derived for HV SNe, and the composition has little trace of the unburnt C+O layer, as in the case of HV SNe.

These properties suggest that the structure of the outermost layer of SN 2012fr, which creates emissions in the very early phase, is similar to that of the HV type. As one moves inward, the inner structure may become more similar to that of the NV type. As such, we suggest that SN 2012fr is placed as a transitional object between the NV and HV classes in the NV–HV sequence.

#### 4.3. SN 2013dy as a Transitional Case in the NV–1991T/1999aa-like Sequence

The other outlier in the NV class is SN 2013dy. While SN 2013dy is classified as an NV SN based on the maximum-

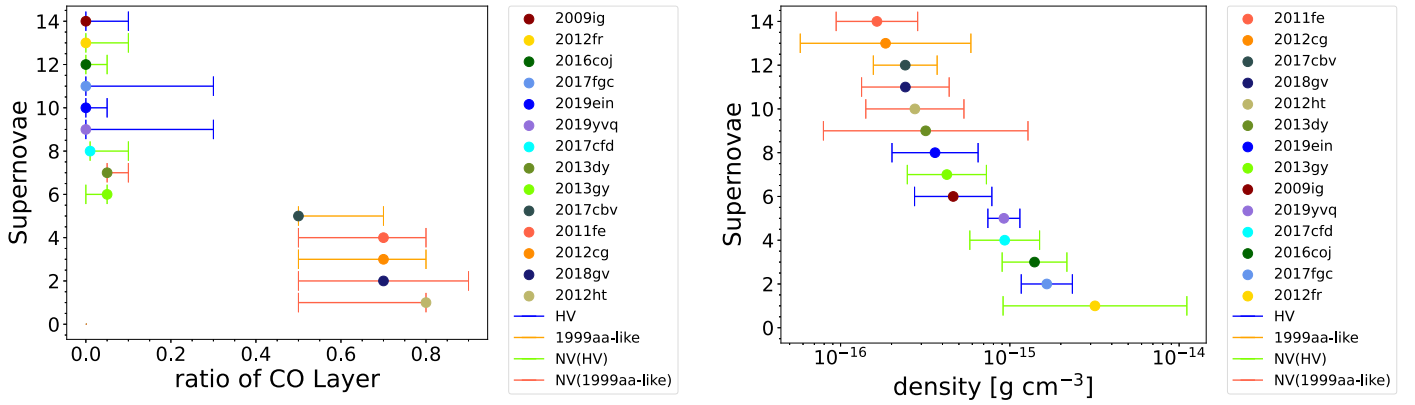


**Figure 7.** Fraction of the CO layer (left) and characteristic density (right) in increasing order from top to bottom. The different subclasses are marked by different colors for the error bars; 999aa-like SNe (orange) and HV SNe (blue), and “C-rich” NV SNe (red) and “C-poor” NV SNe (green).

phase spectra, the outermost density and composition structures derived in this study are very close to those of the 1991T/1999aa-like type. Unlike the other NV SNe (except for SN 2012fr), the ejecta extend to  $\sim 30,000 \text{ km s}^{-1}$ , which is comparable to 1991T/1999aa-like SNe. The density is overall low; it is at the lowest side among NV SNe at the photosphere, and it is comparable to 1991T/1999aa-like SNe in the outermost region. The fraction of the unburnt C+O layer in the outermost layer is  $\sim 0.05$ , which is not as high as those of 1999T-like SNe, but we note that those derived for HV SNe are essentially zero.

These properties suggest that the structure of the outermost layer, as traced in the very early phase, may be similar to those of the 1991T-like type or may represent an intermediate case between 1991T-like and NV SNe. As one moves inward, the inner structure may become more similar to that of the NV type. We note that the photospheric velocity of SN 2013dy in the earliest phase is typical of NV SNe, which is lower than 1991T/1999aa-like SNe. This is consistent with the density structure of SN 2013dy; while the density is comparable to that of 1991T/1999aa-like SNe in the outermost layer, it is overall lower than that of 1991T/1999aa-like SNe toward lower velocities. It is therefore expected that the photosphere is not kept at a high velocity in SN 2013dy.

#### 4.4. Possible Relations to the Explosion Mechanisms

The two possible sequences, the 1991T/1999aa–NV and the HV–NV sequences, indicate that there might exist two distinct progenitor channels and/or explosion scenarios for SNe Ia. In this section, we first discuss the pros and cons of the two popular models, the delayed-detonation model (and the closely related W7 model) and the double-detonation model. The possible relation of each scenario to the different SN Ia populations is discussed. While the content of this section is speculative, we believe that it provides a useful guide for further development, especially in the modeling activity.

Figure 8 shows the comparison between the density structure obtained by the TARDIS spectral synthesis and the  $M_{\text{ch}}$  WD models for which the thermonuclear runaway is triggered in the central region of the WD; the pure-deflagration model W7 (Nomoto et al. 1984) and the delayed-detonation model WS15DD1 (Iwamoto et al. 1999). These two models have similar overall properties in terms of the WD mass (near  $M_{\text{Ch}}$ ), the  $^{56}\text{Ni}$  mass ( $\sim 0.6M_{\odot}$ ), and the explosion energy ( $\sim 1.5 \times 10^{51}$  erg).

For the density structure, the W7 model would not explain the high velocity seen in HV SNe and 1999aa-like SNe. The delayed-detonation model, WS15DD1 as a specific example here, shows that the outermost density structure is largely consistent with those of HV SNe and especially 1999aa-like SNe. The typical density of NV SNe is smaller than those of both models.

However, we note that the direct comparison between the density structures derived by spectral modeling and specific explosion models may be misleading and potentially overstating the discrepancy. SNe Ia show diversity in their peak luminosities, which is interpreted as a result of diversity in the production of  $^{56}\text{Ni}$ . Accordingly, most of the models can produce a variation in the  $^{56}\text{Ni}$  production, where controlling parameters are different for different model sequences (see Section 1). Omitting the details, the difference will translate to the ejecta kinematics through the energy generation, which can lead to a variation in the density structure for a given model sequence. Figure 8 shows this exercise based on the WS15DD1 model, assuming that there is a variation in the kinetic energy of  $\pm 50\%$ <sup>7</sup> and that the ejecta structure responds to the difference in the kinetic energy in a self-similar manner. The model can largely cover the density structures of the sample of SNe Ia<sup>8</sup>, where more energetic models correspond to either 1991T/1999aa-like SNe or HV SNe, while less energetic models cover the density structure derived for NV SNe. Indeed, the explosion energy should be related to the amount of  $^{56}\text{Ni}$  produced in the explosion, in a way that a more energetic SN Ia has a larger amount of  $^{56}\text{Ni}$  and is thus brighter. This expectation is indeed consistent with the idea that a more energetic explosion in the delayed-detonation model may potentially be connected to 1991T/1999aa-like SNe and a less energetic explosion within the same delayed-detonation framework may explain at least a fraction of the NV SNe; this possible link between the observed luminosity sequence and the delayed-detonation scenario has indeed been frequently

<sup>7</sup> This is not an extreme assumption. The mass of  $^{56}\text{Ni}$  has a variation of  $\sim 0.4 - 1M_{\odot}$  or even larger for 1991T-like SNe (e.g., Maeda & Terada 2016, for a review on the SN Ia diversity). If this would trace the variation in the nucleosynthesis products as a whole, the variation in the energy generation rate is more than a factor of 2 (and in principle can be even larger for the final kinetic energy as the binding energy of the WD is to be subtracted).

<sup>8</sup> Note that the variation in the kinetic energy is considered here as a possible source of the variation within the same sequence; this would not create a “distinct” difference between the two sequences.



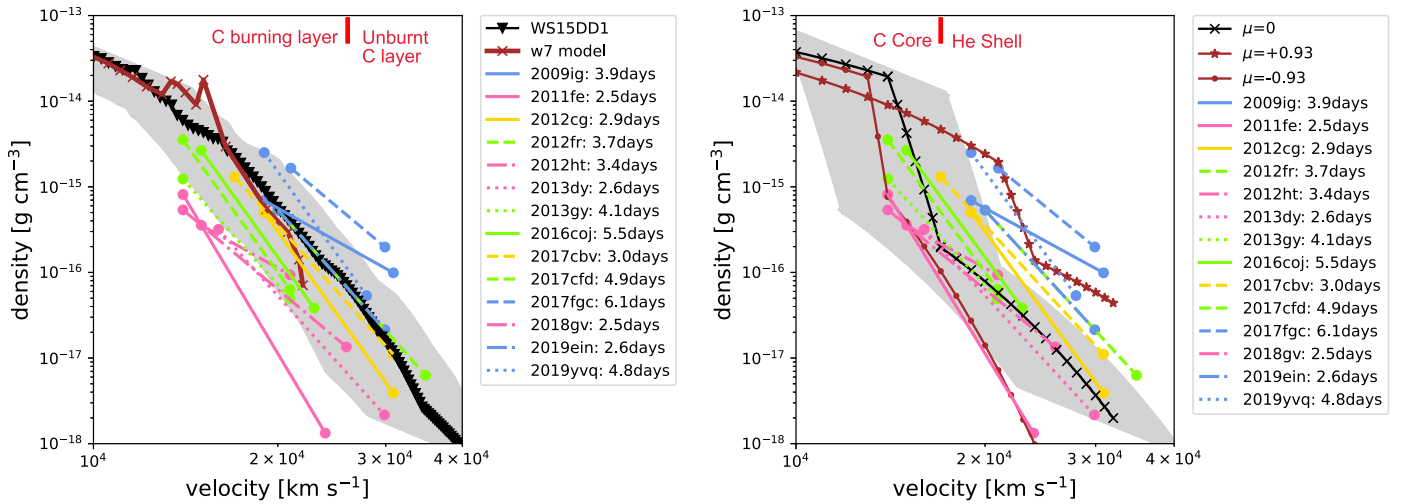


**Figure 8.** Comparison of the density structures obtained by TARDIS to some theoretical models. The left panel shows the W7 model (brown; Nomoto et al. 1984) and the WS15DD1 model (black; Iwamoto et al. 1999); the right panel shows the double-detonation model of Shen et al. (2021), for three choices of the viewing directions (black for  $\mu = 0$  and brown for  $\mu = \pm 0.93$ ). The gray-shaded region shows the trajectory of the WS15DD1 model (left) or the double-detonation model for an average viewing direction ( $\mu = 0$ , right), when the kinetic energy is changed by  $\pm 50\%$ . The vertical red line shows the boundary between different layers (see labels). Different colors are used to show the ejecta structures for individual SNe, depending on the subclasses they belong to; blue lines for the HV SNe and yellow lines for the 1999aa-like SNe. The NV SNe with large and small amounts of the unburnt carbon are denoted by pink and green lines, respectively.

discussed (Mazzali et al. 2014; Zhang et al. 2016a; Ashall et al. 2016).

The amount of unburnt carbon provides additional key constraints. The W7 model has a large amount of unburnt carbon ( $0.032 M_{\odot}$ ), while the WS15DD1 model has  $0.00542 M_{\odot}$ . Apparently, the W7 model predicts that the unburnt carbon mass substantially exceeds the values derived in this work, indicating that detonation should anyway be involved in SN Ia explosions. The amount of unburnt carbon predicted by the WS15DD1 model (or in general the delayed-detonation model) is largely consistent with those found for the “carbon-rich NV–1991T/1999aa sequence.” Given that the delayed-detonation model can also cover the density structure for the sample of SNe Ia including those in this carbon-rich sequence, it survives as a potential model for SNe Ia in the NV–1991T/1999aa sequence.

In the delayed-detonation model sequence of Iwamoto et al. (1999), the unburnt C+O layer exists above  $\sim 25,000 \text{ km s}^{-1}$ . This overlaps with the velocity range for the 1999aa-like SNe where unburnt carbon is found (with an outermost velocity of  $\gtrsim 30,000 \text{ km s}^{-1}$ ). A drawback in this interpretation/scenario is that the ejecta of the (carbon-rich) NV type, for which the unburnt C+O layer is found between  $\sim 15,000 \text{ km s}^{-1}$  and  $\sim 20,000 \text{ km s}^{-1}$ , are found well below the prediction by the delayed-detonation model.

An additional factor that can be a source of observational diversity is the ejecta asymmetry and viewing-angle effect. Given the stochastic nature of the deflagration trigger and the turbulent nature of the deflagration-flame propagation, the delayed-detonation model should have some degree of ejecta asymmetry (Seitenzahl et al. 2013) and even global, one-sided asymmetry (Maeda et al. 2010a, 2011). The density structure, and therefore the Si II velocity, can then be angle-dependent (Maeda et al. 2010b).

Another explosion scenario that deserves consideration is the double-detonation model. Figure 8 shows a comparison between the density structures obtained in the present study and those predicted by the double-detonation model (Shen et al. 2021). In

this model, the carbon core mass and the He shell mass are  $\sim 0.98 M_{\odot}$  and  $\sim 0.016 M_{\odot}$ , respectively.

For the density structure, the double-detonation model is highly dependent on the viewing angle, and the explosion is generally “one-sided” in the most likely situation of the He detonation starting at a single point (Fink et al. 2010). We thus expect a high-density and high-velocity ejecta structure for one side and a low-density and low-velocity ejecta structure for the opposite direction. This behavior is seen in the model by Shen et al. (2021), and a possible association of the different viewing angles to different subclasses is indicative; the ejecta density in the “high-velocity” side ( $\mu = +0.93$ ) roughly matches the structure of either 1991T/1999aa-like SNe Ia or HV SNe Ia, while that in the “low-velocity” to “average-velocity” sides ( $\mu = -0.93$  to 0) resembles that of NV SNe.<sup>9</sup>

The unburnt carbon masses in the carbon core and the He shell are  $0.0041 M_{\odot}$  and  $0.00013 M_{\odot}$ , respectively. The interface between the core and the shell is around the jump in the density structure. In Figure 8, it is seen that the velocity range as probed by the TARDIS model results basically corresponds to the He shell. Therefore, in this particular model, the He shell is mostly observed with a minor contribution from the core materials. The amount of the unburnt carbon in the He shell is very small, which contradicts that found for the SNe in the 1991T/1999aa–NV (C-rich and low-density) sequence. On the other hand, the model prediction on the carbon mass provides a qualitative match to the carbon-poor ejecta found for (most of) the SNe in the HV–NV (C-poor and high-density) sequence.

As in the case of the delayed-detonation model (see above), the density structure should be dependent on the energy production (and the WD mass). Thus, this may provide an additional possibility to connect the HV–NV sequence in terms of the expected variation in the energy generation as mainly determined by the WD mass in this scenario. Additionally, the density in the He shell will also be affected by the amount of

<sup>9</sup> This is indeed a qualitatively similar argument based on an asymmetric delayed-detonation model to explain the HV and NV classes by the viewing-angle effect (Maeda et al. 2010b).

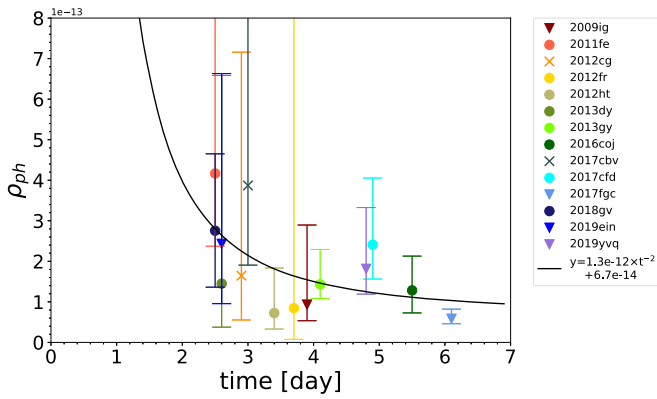


**Figure 9.** Density at the photosphere for the sample of SNe Ia at different epochs. The black line is the curve described by  $t^{-2}$ . Different symbols are used for different subclasses (see the caption of Figure 5).

the He shell. Omitting the details and just assuming the variation in the kinetic energy by  $\pm 50\%$  with a fixed WD mass, we can roughly reproduce a range of the density structure covering both NV and HV SNe, considering that the variation in the viewing direction will introduce further diversity. Additional effects of the change in the progenitor WD mass and the He shell mass should further widen the expected range so that the range of the density structure derived with the TARDIS models may easily be explained. However, this effect should not be a main driver to creating the difference within the HV–NV sequence; little difference is seen in the luminosities of HV SNe and NV SNe, while the energy generation affects the  $^{56}\text{Ni}$  production.

In summary, we tentatively conclude that the 1991T/1999aa–NV sequence and the HN–NV sequence might be linked to the delayed-detonation mechanism and the double-detonation mechanism. The transition of the SN subclass in the 1991T/1999aa–NV sequence could be explained by the strength of the nuclear burning, forming the peak-luminosity sequence. On the other hand, the difference between the HV and NV SNe within the HV–NV sequence should not be explained by a similar effect, and the highly asymmetric ejecta and the viewing-angle effect may be a possible factor to form this sequence. Note that there are also some problems that are not readily explained by the scenario provided here; for example, the outermost ejecta density predicted in the reference models used for the comparison is indeed higher for the delayed-detonation model than the double-detonation model, while the present study indicates the higher density for the HV–NV sequence than for the 1991T/1999aa–NV sequence.

## 5. Discussion

### 5.1. Density at the Photosphere

Figure 9 shows the density at the photosphere, obtained for the best-fit models for the sample of spectra at different epochs. Overplotted by a black line is the curve described by  $t^{-2}$ , which roughly represents the evolution of the density at which the optical depth is unity if the Rosseland mean opacity is taken to be constant with time. Overall, the photospheric densities found for the early phase (within a week since the explosion) are clustered in the range between  $\sim 6 \times 10^{-14} [\text{g cm}^{-3}]$  and  $\sim 7 \times 10^{-13} [\text{g cm}^{-3}]$ ; while the errors for individual measurements can be large for some data points, the evolution is consistent with the  $t^{-2}$  curve.

It might indicate that the location of the photosphere depends on the density at that point but is not sensitive to the temperature or the density outside it. This is expected for the following reason; in the very early phase, the density gradient is so steep that the continuum optical depth is mainly contributed by a small region just above the photosphere. What is not trivial is that the position of the photosphere is relatively insensitive to the temperature there, which is obtained as a result of the spectral formation computed by TARDIS as calibrated with the observed spectra. This indicates that a constant opacity is not a bad approximation to evaluate the position of the photosphere, despite the range of the photospheric temperature derived for different SNe Ia (Section 5.2).

### 5.2. The Photospheric Temperature and the “Early-phase” Branch Diagram

An established way to investigate the diversity in SNe Ia is the Branch diagram (Branch et al. 2006), specifically developed based on the maximum-phase properties. The diagram provides a guide in studying the origin of spectral diversity (e.g., Nugent et al. 1995). Now that we have extracted the physical properties of the outermost ejecta, we are motivated to produce an analog of the Branch diagram but for the earliest phase and investigate the possible origin of the observed diversity. In addition, expanding the Branch diagram to various phases is interesting on its own; such an investigation has been rare so far, especially for the earliest phase due to the paucity of the data. In this section, we first present an early-phase version of the Branch diagram (i.e., the spectral properties) and investigate how it is related to the decline rate (i.e., the light-curve properties) and then to the photospheric temperature (i.e., the outcome of the spectral modeling).

#### 5.2.1. Branch-like Diagram using Very-early-phase Observables

Figure 10 shows an early-phase version of the Branch diagram (Branch et al. 2006). In our sample we have two 1999aa-like SNe, which are classified as the “shallow-silicon” class based on their maximum-light spectra showing small EWs of both Si II 5972 Å and Si II 6355 Å. In the early-phase spectra (within a week since the explosion), they show the same behavior and can be distinguished from other subclasses in the same manner with the maximum-light classification scheme. Interestingly, the opposite is not the case; we see that SN 2013dy, which is classified as the “core-normal” class (which is nearly identical to the “NV” classification) in the maximum phase, does show the shallow-silicon characteristics in the early, rising phase. Namely, it should be categorized into the same group as the 1991T/1999aa-like subclass (or shallow-silicon class) in the very early phase, which is consistent with the result of the TARDIS modeling (see Section 4.3).

HV SNe are distinguished from other subclasses by their large EWs of Si II 6355 Å in the maximum-phase Branch diagram. Figure 10 shows that the same applies to their early-phase spectra. For HV SNe except for 2019yvq, the EWs of Si II 6355 Å are larger than 100 Å and those shown by the other subclasses. Similar to the case for the 1991T/1999aa-like subclass, there is a transitional object, which changes its spectral properties; SN 2012fr is in the NV (or core-normal) subclass based on the maximum-phase classification, but it

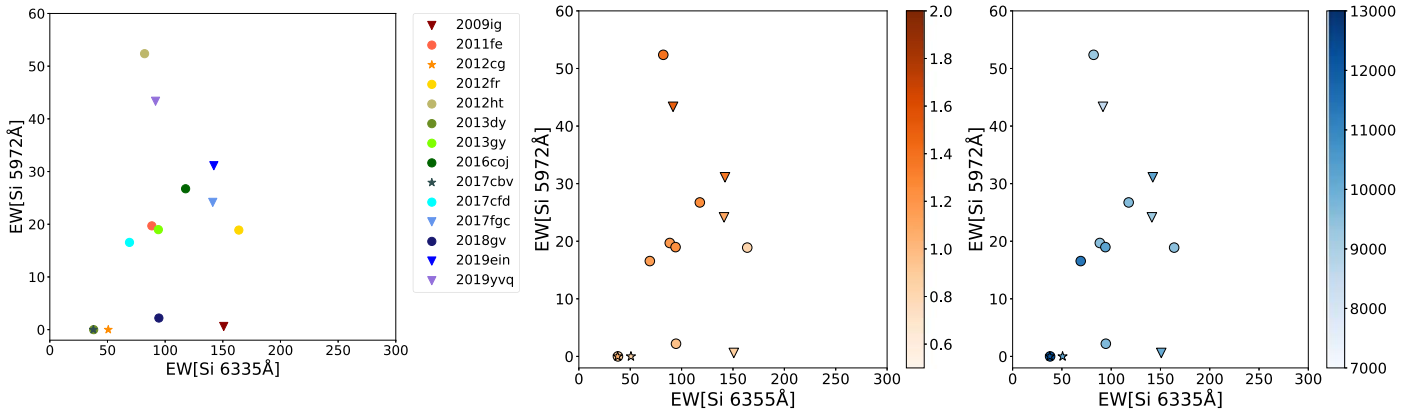


**Figure 10.** Analog of the Branch diagram for the very-early-phase spectra we used (left). Circles represent the NV type, inverse triangles indicate the HV type, and stars correspond to the 1999aa-like type. The same figure but marked with  $\Delta m_{15}$  is shown in the middle panel; the colors of the symbols indicate the values of  $\Delta m_{15}$  following the color bar on the right side. The same but marking the photospheric temperature is shown in the right panel.

clearly shares the spectral properties with HV SNe in the very early phase (see Section 4.2).

For most NV SNe, the EWs of Si II 5972 Å and Si II 6355 Å are around 20 Å and 80 Å, respectively. This is separated from the region occupied by the 1991T/1999aa-like and HV SNe, and thus they share their identity as the NV class even in the very early phase. As mentioned above, the opposite is not the case; we see a few examples that turn their properties either from the 1991T/1999aa-like class or the HV class to the NV class toward the maximum phase, while in our sample we do not see clear examples of the opposite case, i.e., a transition from the NV class to the other classes.

In summary, we conclude that the classification based on the maximum-light spectra generally holds in the very-early-phase observable. Interestingly, a fraction of SNe change their classifications depending on the spectral phase (i.e., SN 2012fr, SN 2013dy), from the 1991T/1999aa-like class or the HV class to the NV class (but not the opposite); this can be understood in view of their ejecta structures, as derived by the TARDIS modeling, bridging different subclasses in the outer and inner regions.

### 5.2.2. Dependence on the Declining Rate

In terms of  $\Delta m_{15}$ , the very-early-phase Branch diagram may provide stronger diagnostics than in the maximum-light phase. Figure 10 shows the  $\Delta m_{15}$  distribution. For HV SNe, there is a clear trend that SNe with larger  $\Delta m_{15}$  are distributed in the upper region (i.e., a larger EW of Si II 5972 Å). The same tendency can be seen for NV SNe. This behavior is especially clear for SN 2012ht and SN 2019yvq, whose  $\Delta m_{15}$  is very large. They are distributed in the uppermost portion of the diagram, which may be analogous to the “cool”-type classification in the maximum-light phase. While the cool type (or SN 1991bg-like SNe) is not included in our sample, it might indeed represent a transitional case from the 1991bg-like (cool) subclass in the early phase to the NV (core-normal) subclass in the maximum-light phase. Adding a sample of 1991bg-like SNe in the rising phase is strongly encouraged to confirm this suggestion. For the shallow-silicon type,  $\Delta m_{15}$  tends to be small; this type indeed occupies the lowest portion in this diagram.

### 5.2.3. Dependence on the Temperature

Nugent et al. (1995) investigated the origin of the spectral classification and showed that the photospheric temperature is a key quantity that controls the spectral properties along the luminosity sequence in the maximum-light phase. For high temperatures, the EW of Si II 6355 Å is small and the Si II 5972 Å line is rarely detectable. For temperatures between 8600 and 9800 K, both the Si II 5972 Å and Si II 6355 Å lines become strong. For the temperature under 8000 K, the EW of Si II 5972 Å increases to become comparable to or even stronger than the 6355 Å line.

Figure 10 shows the photospheric temperature distribution in the very early phase calculated by TARDIS on the (early-phase) Branch diagram. There is a clear trend between the temperature and the EWs of these lines, linking the SNe showing the higher EWs to the lower temperature. The trend is especially strong in the EW of Si II 5972 Å; this corresponds to the temperature sequence found by Nugent et al. (1995) for the maximum-light spectra. We note that the two SNe with the strongest Si II 5972 Å are indeed not the “cool-type” SNe in the maximum-light classification, but they might be classified as an analog of the cool type (1991bg-like) in the very early phase and transitions to other subclasses in the maximum light (see above). HV SNe (or BL type) show relatively low temperatures in the early rising phase, which is analogous to the low temperature derived for them based on the maximum-light spectra (Hachinger et al. 2008; Tanaka et al. 2008).

### 5.3. Rise Time

Figure 11 shows the relation between the time since the explosion and the luminosity, which are both obtained by the spectral fitting with TARDIS, as shown by the symbols. The TARDIS points are used to anchor the *r*- or *R*-band light curves of the same objects shown by the lines with the same colors as the TARDIS points. There is a clear tendency for objects with lower  $\Delta m_{15}$  to show higher luminosity in the early rising phase. This is mainly explained by the difference in the peak luminosity, in a way that SNe that are bright in the maximum phase tend to be bright also in the early phase. This is naturally expected from the relation between the peak luminosity and the peak date.

SNe 1991T/1999aa-like SNe show small  $\Delta m_{15}$  and thus high peak luminosities; they are thus on the top portion in the



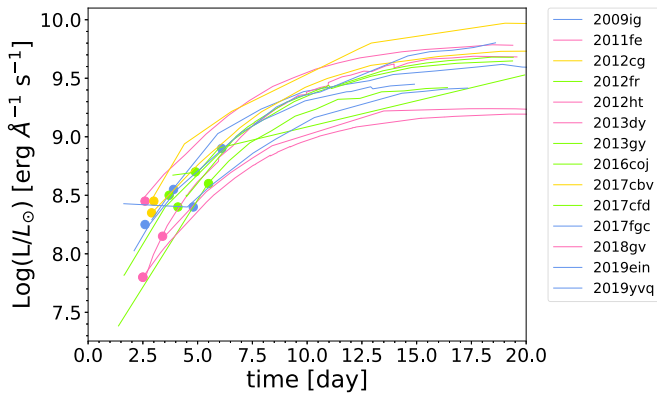


**Figure 11.** Relation between the time since the explosion and luminosity. The symbols represent the results of the TARDIS modeling. This is overlapped with the  $R$ - or  $r$ -band light curve for each object. Different colors are used for different subclasses (see the caption of Figure 8). Note that SN 2011fe is hidden behind SN 2018gv.

luminosity in the rising phase. No clear trend is seen about the rising luminosities and the other subclasses, i.e., the HV and NV SNe (in which the latter may be further divided into C-rich and C-poor) are not readily distinguishable, showing little trend beyond what the  $\Delta m_{15}$  values would predict. The analysis here suggests two points in coordinating follow-up observations; (1) to study the early-phase “excess,” one has to obtain highly sampled multiband light curves (Burke et al. 2022), as a single point that is calibrated by the spectral modeling does not help much to search for the early excess. (2) Oppositely, to extract the overall physical properties, a single spectrum can be more powerful than high-cadence photometric observations.

## 6. Conclusions

Aiming at constraining the explosion mechanisms, we have modeled very-early-phase spectra of 14 SNe Ia. By using the one-dimensional Monte Carlo radiation transfer code, TARDIS, we have estimated the density structure and composition structure of the outermost ejecta. We have introduced a semi-automatic fitting method to evaluate the quality of the fit between the synthesized and observed spectra, which enhances the reproducibility as well as allows us to evaluate the uncertainty in the derived parameters.

We find that the outermost density structure is different for different subclasses. The HV type has a high density in the outermost layer, which extends to  $\sim 30,000 \text{ km s}^{-1}$ . The SN1999aa-like type shows the outermost ejecta extending to a similar velocity ( $\sim 30,000 \text{ km s}^{-1}$ ), but with the density preferentially lower than in the HV class. The NV type does not show the high ejecta velocity found in the other classes; they are mostly limited to  $\sim 20,000 \text{ km s}^{-1}$ . The densities of the ejecta between the photosphere ( $\sim 15,000 \text{ km s}^{-1}$ ) and the outermost layer ( $\sim 20,000 \text{ km s}^{-1}$ ) of the NV SNe show substantial diversity of nearly an order of magnitude.

We have also shown that the composition structures are divided into two groups; those dominated by the unburnt C + O-rich layer and those dominated by the carbon-burning layer with little trace of the unburnt C + O layer. Interestingly, the 1991T/1999a-like SNe and the HV SNe are clearly divided in this composition structure; C-rich for the 1991T/1999a-like class and C-poor for the HV class. The NV class shows diversity; some show C-rich composition while others show

C-poor composition. There is a tendency for C-rich NV SNe to show lower density than C-poor NV SNe.

According to these investigations, we suggest that the NV SNe may indeed be divided into two classes, one connected to the 1991T/1999aa-like class and the other to the HV class. Namely, the whole SN Ia sample analyzed here may be categorized into two populations; one with a C-rich and low-density outermost layer (the 1991T/1999aa-like class and some NV SNe) and the other with a C-poor and high-density outermost layer (the HV class and other NV SNe). Accordingly, the SNe may be divided into two sequences.

These two sequences are likely associated with different origins in their progenitors and explosions. As one possibility, we have discussed how the two popular scenarios, the delayed-detonation mechanism on a  $M_{\text{Ch}}$  WD and the double-detonation on a sub- $M_{\text{Ch}}$  WD, could explain the properties of the ejecta as derived by the TARDIS modeling for different sequences and subclasses. One possibility is this; the delayed-detonation mechanism is associated with the 1991T/1999aa–NV (C-rich and low-density) sequence, where the strength of the burning may control a transition between 1991T/1999aa-like SNe and NV SNe; the double-detonation mechanism is associated with the HV–NV (C-poor and high-density) sequence, where the viewing angle may be a driving factor to create the transition between HV and NV SNe.

We have also plotted the early-phase spectral properties in the very early phase, in the same manner as the Branch diagram established for the maximum-light properties. Different subclasses form different sequences in this diagram, similar to what is found for the maximum-phase properties. As in the maximum-light phase, the different subclasses can be characterized mainly by the photospheric temperature, while the HV class shows a relatively large diversity in the temperature. Interestingly, there is one NV SN that has similar properties with the 1991T/1999aa-like class in the early-phase Branch diagram and one NV SN that is indistinguishable from HV SNe. These “transitions” indicate that the SNe have outermost ejecta properties that are more closely related to other subclasses than the NV class. Namely, the outermost ejecta of the NV class show larger diversity than the inner ejecta. Furthermore, the NV SN (2013dy), which shows the transition from the 1991T/1999-like to the NV class, is indeed in the C-rich, low-density sequence (i.e., the 1991T/1999aa–NV sequence), and the NV SN (2012fr), which shows the transition from the HV class to the NV class, is in the C-poor, high-density sequence (i.e., the HV–NV sequence). This strengthens our argument for the existence of the two sequences. Interestingly, we have not identified the opposite transition, i.e., a transition of the NV class to either the 1991T/1999a-like class or the HV class. In addition, the early-phase Branch diagram suggests that one HV and one NV might be considered as early-phase analogs of the “cool” (1991bg-like) class, further pointing to the same picture.

## Acknowledgments

The authors thank Daichi Hiramatsu, Jian Jiang, Masaomi Tanaka, and Kohki Uno for stimulating discussions. K.M. acknowledges support from the Japan Society for the Promotion of Science (JSPS) KAKENHI grants JP18H05223 and JP20H00174. Numerical computations for this work were carried out at the Yukawa Institute Computer Facility. Some data presented in this work were obtained from WISeREP



(<https://www.wiserep.org>). This research made use of TARDIS, a community-developed software package for spectral synthesis in supernovae. The development of TARDIS received support from GitHub, the Google Summer of Code initiative, and ESA's Summer of Code in Space program. TARDIS is a fiscally sponsored project of NumFOCUS. TARDIS makes extensive use of Astropy and Pyne.

*Software:* TARDIS v2022.06.19 (Kerzendorf & Sim 2014).

### ORCID iDs

Mao Ogawa  <https://orcid.org/0000-0001-5822-1672>

Keiichi Maeda  <https://orcid.org/0000-0003-2611-7269>

Miho Kawabata  <https://orcid.org/0000-0002-4540-4928>

### References

- Aouad, C. J., Mazzali, P. A., Hachinger, S., et al. 2022, *MNRAS*, 515, 4445
- Arnett, W. D. 1982, *ApJ*, 253, 785
- Ashall, C., Mazzali, P. A., Pian, E., & James, P. A. 2016, *MNRAS*, 463, 1891
- Barna, B., Pereira, T., Taubenberger, S., et al. 2021, *MNRAS*, 506, 415
- Benetti, S., Cappellaro, E., Mazzali, P. A., et al. 2005, *ApJ*, 623, 1011
- Berton, M., Bufano, F., Floers, A., et al. 2018, *TNSCR*, 2018-2076, 1
- Branch, D., Dang, L. C., Hall, N., et al. 2006, *PASP*, 118, 560
- Burgaz, U., Maeda, K., Kalomeni, B., et al. 2021, *MNRAS*, 502, 4112
- Burke, J., Howell, D. A., Sand, D. J., et al. 2022, arXiv:2207.07681
- Burke, J., Howell, D. A., Sarbadhicary, S. K., et al. 2021, *ApJ*, 919, 142
- Cain, C., Baron, E., Phillips, M. M., et al. 2018, *ApJ*, 869, 162
- Cardelli, J. A., Clayton, G. C., & Mathis, J. S. 1989, *ApJ*, 345, 245
- Childress, M. J., Scalzo, R. A., Sim, S. A., et al. 2013, *ApJ*, 770, 29
- Contreras, C., Phillips, M. M., Burns, C. R., et al. 2018, *ApJ*, 859, 24
- De, K., Kasliwal, M. M., Polin, A., et al. 2019, *ApJL*, 873, L18
- Filippenko, A. V., Richmond, M. W., Branch, D., et al. 1992b, *AJ*, 104, 1543
- Filippenko, A. V., Richmond, M. W., Matheson, T., et al. 1992a, *ApJL*, 384, L15
- Fink, M., Röpke, F. K., Hillebrandt, W., et al. 2010, *A&A*, 514, A53
- Foley, R. J., Challis, P. J., Filippenko, A. V., et al. 2012, *ApJ*, 744, 38
- Hachinger, S., Mazzali, P. A., Tanaka, M., Hillebrandt, W., & Benetti, S. 2008, *MNRAS*, 389, 1087
- Han, X., Zheng, W., Stahl, B. E., et al. 2020, *ApJ*, 892, 142
- Heringer, E., van Kerkwijk, M. H., Sim, S. A., Kerzendorf, W. E., & Graham, M. L. 2019, *ApJ*, 871, 250
- Hoefflich, P., & Khokhlov, A. 1996, *ApJ*, 457, 500
- Holmbo, S., Stritzinger, M. D., Shappee, B. J., et al. 2019, *A&A*, 627, A174
- Hosseinzadeh, G., Sand, D. J., Valenti, S., et al. 2017, *ApJL*, 845, L11
- Iben, I., & Tutukov, A. V. J. 1984, *ApJ*, 284, 719
- Iwamoto, K., Brachwitz, F., Nomoto, K., et al. 1999, *ApJS*, 125, 439
- Iwata, K., & Maeda, K. 2022, *ApJ*, 941, 87
- Jiang, J.-A., Doi, M., Maeda, K., et al. 2017, *Natur*, 550, 80
- Kasen, D. 2006, *ApJ*, 649, 939
- Kawabata, M., Maeda, K., Yamanaka, M., et al. 2020, *ApJ*, 893, 143
- Kerzendorf, W. E., & Sim, S. A. 2014, *MNRAS*, 440, 387
- Kerzendorf, W. E., Vogl, C., Buchner, J., et al. 2021, *ApJL*, 910, L23
- Khokhlov, A. M. 1991, *A&A*, 245, 114
- Kwok, L. A., Williamson, M., Jha, S. W., et al. 2022, *ApJ*, 937, 40
- Li, W., Wang, X., Bulla, M., et al. 2021, *ApJ*, 906, 99
- Maeda, K., Benetti, S., Stritzinger, M., et al. 2010, *Natur*, 466, 82
- Maeda, K., Jiang, J.-a., Shigeyama, T., & Doi, M. 2018, *ApJ*, 861, 78
- Maeda, K., Leloudas, G., Taubenberger, S., et al. 2011, *MNRAS*, 413, 3075
- Maeda, K., Röpke, F. K., Fink, M., et al. 2010a, *ApJ*, 712, 624
- Maeda, K., & Terada, Y. 2016, *IJMPD*, 25, 1630024
- Magee, M. R., Kotak, R., Sim, S. A., et al. 2017, *A&A*, 601, A62
- Mazzali, P. A., Sullivan, M., Hachinger, S., et al. 2014, *MNRAS*, 439, 1959
- Miller, A. A., Magee, M. R., Polin, A., et al. 2020, *ApJ*, 898, 56
- Meng, X., Zhang, J., & Han, Z. 2017, *ApJ*, 841, 62
- Modjaz, M., Liu, Y. Q., Bianco, F. B., & Graur, O. 2016, *ApJ*, 832, 108
- Nasonova, O. G., de Freitas Pacheco, J. A., & Karachentsev, I. D. 2011, *A&A*, 532, A104
- Nomoto, K. 1982, *ApJ*, 257, 780
- Nomoto, K., Thielemann, F. K., & Yokoi, K. 1984, *ApJ*, 286, 644
- Nugent, P., Phillips, M., Baron, E., Branch, D., & Hauschildt, P. 1995, *ApJL*, 455, L147
- O'Brien, J. T., Kerzendorf, W. E., Fullard, A., et al. 2021, *ApJL*, 916, L14
- O'Brien, J. T., Kerzendorf, W. E., Fullard, A., et al. 2023, arXiv:2306.08137
- Pan, Y. C., Foley, R. J., Kromer, M., et al. 2015, *MNRAS*, 452, 4307
- Pellegrino, C., Howell, D. A., Sarbadhicary, S. K., et al. 2020, *ApJ*, 897, 159
- Perlmutter, S., Aldering, G., Goldhaber, G., et al. 1999, *ApJ*, 517, 565
- Phillips, M. M. 1993, *ApJL*, 413, L105
- Riess, A. G., Filippenko, A. V., Challis, P., et al. 1998, *AJ*, 116, 1009
- Röpke, F. K., Hillebrandt, W., Schmidt, W., et al. 2007, *ApJ*, 668, 1132
- Seitenzahl, I. R., Ciaraldi-Schoolmann, F., Röpke, F. K., et al. 2013, *MNRAS*, 429, 1156
- Shen, K. J., Boos, S. J., Townsley, D. M., & Kasen, D. 2021, *ApJ*, 922, 68
- Shen, K. J., Kasen, D., Miles, B. J., & Townsley, D. M. 2018, *ApJ*, 854, 52
- Silverman, J. M., Ganeshalingam, M., Cenko, S. B., et al. 2012, *ApJL*, 756, L7
- Sim, S. A., Röpke, F. K., Hillebrandt, W., et al. 2010, *ApJL*, 714, L52
- Tanaka, M., Mazzali, P. A., Benetti, S., et al. 2008, *ApJ*, 677, 448
- Tanikawa, A., Nomoto, K., & Nakasato, N. 2018, *ApJ*, 868, 90
- Umeda, H., Nomoto, K., Yamaoka, H., & Wanajo, S. 1999, *ApJ*, 513, 861
- Wang, X., Filippenko, A. V., Ganeshalingam, M., et al. 2009, *ApJL*, 699, L139
- Whelan, J., & Iben, I. J. 1973, *ApJ*, 186, 1007
- Woosley, S. E., & Kasen, D. 2011, *ApJ*, 734, 38
- Yamanaka, M., Maeda, K., Kawabata, M., et al. 2014, *ApJL*, 782, L35
- Yang, Y., Hoefflich, P., Baade, D., et al. 2020, *ApJ*, 902, 46
- Yaron, O., & Gal-Yam, A. 2012, *PASP*, 124, 668
- Zhang, J.-J., Wang, X.-F., Sasdelli, M., et al. 2016a, *ApJ*, 817, 114
- Zhang, K., Wang, X., Zhang, J., et al. 2016b, *ApJ*, 820, 67
- Zhao, X., Wang, X., Maeda, K., et al. 2015, *ApJS*, 220, 20
- Zheng, W., Filippenko, A. V., Mauerhan, J., et al. 2017, *ApJ*, 841, 64
- Zheng, W., Silverman, J. M., Filippenko, A. V., et al. 2013, *ApJL*, 778, L15